

# Electrical post-fabrication tuning of aluminum Josephson junctions at room temperature

Christian Križan<sup>\*,1</sup>, Maurizio Toselli<sup>\*,1,‡</sup>, Irshad Ahmad<sup>1</sup>, Hadi Khaksaran<sup>1</sup>, Marcus Rommel<sup>1</sup>, Nermin Trnjanin<sup>1</sup>, Janka Biznárová<sup>1</sup>, Mamta Dahiya<sup>1</sup>, Emil Hogedal<sup>1</sup>, Halldór Jakobsson<sup>1</sup>, Andreas Nylander<sup>1</sup>, Jonas Bylander<sup>1</sup>, Per Delsing<sup>1</sup>, Giovanna Tancredi<sup>1</sup>

<sup>1</sup> Department of Microtechnology and Nanoscience, Chalmers University of Technology, SE-412 96 Gothenburg, Sweden

E-mail: krizan@chalmers.se and christian.krizan@gmail.com

\* These authors contributed equally to this work.

February 2026

**Abstract.** Josephson junctions are a key element of superconducting quantum technology, serving as the core building blocks of superconducting qubits. We present an experimental study on room-temperature electrical tuning of aluminum junctions, showing that voltage pulses can controllably increase their resistance and adjust the Josephson energy while maintaining qubit quality factors above 1 million. We find that the rate of resistance increase scales exponentially with pulse amplitude during manipulation, after which the spontaneous resistance increase scales proportionally to the amount of manipulation. We show that this spontaneous increase halts at cryogenic temperatures, and resumes again at room temperature. Using our stepwise protocol, we achieve up to a 270% increase in junction resistance, corresponding to a reduction of nearly 2 GHz of the qubit transition frequency. These results establish the achievable range, relaxation behavior, and practical limits of electrical tuning, enabling post-fabrication mitigation of frequency crowding in quantum processors.

*Keywords:* amorphous materials, electrical tuning, frequency crowding, Josephson junctions, superconducting circuits, qubit

## 1. Introduction

Quantum processors promise to tackle computational tasks far beyond those of classical computers, with superconducting architectures [1] leading the way. Yet, their practical realization remains constrained by persistent fabrication challenges in the nanoscopic precision required to produce reliable qubits. The key element of any superconducting

‡ Present address: Silicon Quantum Computing Pty Ltd., UNSW Sydney, New South Wales, Australia

qubit is the Josephson junction [2, 3], most commonly fabricated by connecting two superconducting leads by a thin dielectric oxide. The qubit transition frequencies are determined by junction properties such as its normal state resistance and its reactive environment, and can thus be engineered during the design stage. Despite advancements in the fabrication of Josephson junctions in terms of improvements in lithography, junction deposition, oxidation, evaporation, and angular deposition techniques [4–8], the state-of-the-art junction resistance spread is on the order of 2% [9] across a 50 mm wafer, corresponding to a frequency spread of about  $\pm 50$  MHz for transmon qubits. Frequency imprecision translates into spectral collisions between quantum operations [10], that is, frequency crowding. For processors with as few as  $\sim 30$  qubits, frequency crowding can reduce the probability of collision-free operations to below single-digit percentages [6, 11]. Scaling further to 1000 qubits is projected to demand frequency placement with only a few MHz of tolerance [11]. These fabrication constraints motivated the development of post-fabrication tuning techniques for Josephson junctions, where the junction resistance is modified to reach the desired qubit frequencies.

Almost universally, approaches to tuning the Josephson junction resistance rely on heating [12, 13]. Thermal annealing below 250 °C is generally believed to increase the resistance by growing the oxide layer using already-present chemisorbed oxygen [12, 13] or hydroxyl groups [12], with the contribution from hydroxyl groups likely to be smaller [13]. At higher annealing temperatures, the barrier growth is primarily driven by oxygen diffusion [12]. Through thermal annealing, resistance increases up to 400% and 290% have been reported for  $4 \mu\text{m}^2$  Nb-AlO<sub>x</sub>-Nb junctions [13] and Al-AlO<sub>x</sub>-Al junctions [14], respectively. However, thermally annealing a whole quantum processor does not allow for selectively tuning the resistance of individual junctions. This limitation pushed development towards laser annealing [10, 15, 16], which can achieve a tuning range of 15% [11, 17] within tens of seconds [11] at a success rate of about 90% [17] with a 0.3% resistance spread. Lately, electron beam heating [18] has been used to anneal junctions, demonstrating lower tuning ranges of 3% with approximately 1.5% resistance spread [19].

A rapidly growing interest is now directed towards electrical tuning, where the resistance of an individual Josephson junction is modified by applying electrical pulses to its electrodes [20–22]. Applying pulses that alternate in polarity significantly enhances the resistance increase [22], with changes shown exceeding 130% [23]. These recent demonstrations underscore electrical tuning as a promising candidate for precise and selective post-fabrication tuning of superconducting qubits, motivating an investigation into its mechanisms, limits, and feasibility for fine-tuning quantum processors.

A practical complication of electrical tuning is the junction’s relaxation effect. At room temperature, once the tuning process is stopped, the junction resistance does not remain at its tuned value. Instead, it increases rapidly and continues to drift with a slow decay lasting several hours. For frequency targeting in real quantum processors, this effect implies that the tuning process cannot simply be stopped when the desired resistance is reached. Therefore, reliable tuning requires a quantitative understanding

of this relaxation effect.

In this work, we investigate the performance and limitations of electrical tuning. We characterize the natural aging of Josephson junctions, observing a gradual increase in junction resistances over time, and show that routine resistance measurements do not affect aging. We find that the rate of resistance change scales exponentially with the applied tuning voltage. We demonstrate that with our tuning procedure, performed entirely at room temperature, we achieve almost 100% resistance increase in 5 min. We investigate the effects of repeated tuning cycles and demonstrate cumulative resistance increases of up to 270%. We characterize the spontaneous post-manipulation resistance increase that follows the electrical tuning, and show that it scales linearly with the intentionally induced resistance change. Finally, we assess the impact of the manipulation process on transmon qubits [24] subjected to frequency tuning, and find qubit quality factors preserved above one million.

## 2. Experimental procedures and sample information

We investigate electrical tuning in three variants of Josephson junctions fabricated on separate wafers using distinct fabrication processes. The junctions are classified as *low-dose*, *medium-dose*, and *high-dose*, corresponding to the increasing oxidation doses employed during junction fabrication. Each wafer contains hundreds of junctions across 10 cross-sectional areas, with electrode widths from 150 nm to 600 nm. On the *low-dose* wafer, the electrode widths span 100 nm to 550 nm.

The fabrication process is described in [25]. It is important to note that our fabrication processes include multiple baking steps after Josephson junction deposition. Previous work [22] has shown that heating modifies the resistance tunability of Josephson junctions. Thermal annealing of Nb-AlO<sub>x</sub>-Nb junctions has been reported for temperatures and durations comparable to those experienced by our samples [13]. We therefore expect post-deposition heating to influence the tuning behavior observed here, although its quantitative impact is not addressed in this work.

The post-deposition heating consist of lift-off at 85 °C for 150 min, resist baking for patch lithography totaling 160 °C for 15 min, patch lift-off at 85 °C for 180 min, dicing-protective resist baking at 100 °C for 1 min, and a final resist removal at 85 °C for 15 min. The *low-dose* junctions were fabricated using the PICT process [26], in which the patch-related steps are removed. The *medium-dose* wafer contains airbridges, and is thus subjected to four yet additional heating steps: resist baking for lithography at 115 °C for 90 s, resist reflow at 160 °C for 4 min, additional resist baking for lithography and dicing totaling 100 °C for 100 s, and resist removal totaling 90 °C for 20 min. The *low-dose* and *medium-dose* junctions were deposited using a Plassys MEB550S evaporator, and the *high-dose* junctions were deposited in a Plassys MEB550SL3-UHV.

## 2.1. Active resistance manipulation

While junctions naturally age through a passive process in which the resistance increases spontaneously over time, the resistance can also be intentionally manipulated. We refer to this process as *active* resistance manipulation. We modify the junction resistances using a bipolar voltage pulse train comprising a positive-bias square pulse, a blanking interval, a negative-bias square pulse, and a second blanking interval of equal duration. The protocol closely follows the alternating-bias assisted annealing technique, with minor differences in probing and measurement [22]. We show our standard pulse sequence in figure 1(a), with figure 1(b) being an example of active resistance manipulation. No substrate heating is applied during these experiments; thermal effects are discussed separately in section Appendix F.

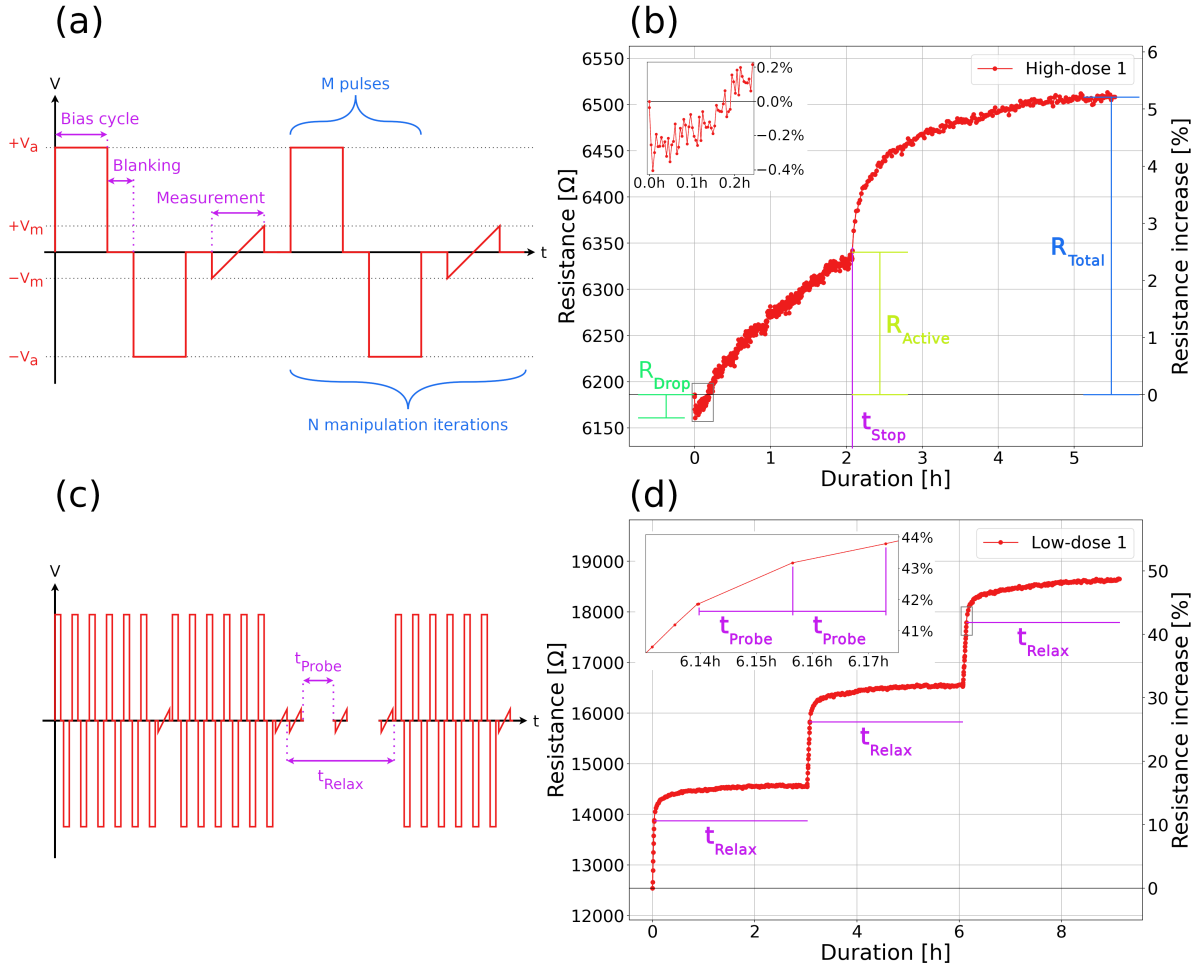


**Figure 1.** Active resistance manipulation of a Josephson junction using two different sequences of voltage pulses. (a) Schematic illustration of the *active* resistance manipulation protocol. (b) An example resistance trace of a junction manipulated up to the time  $t_{\text{Stop}}$  with the scheme in (a), showing the initial resistance drop, active manipulation, and subsequent relaxation. The inset shows a magnified view of the initial resistance drop. (c) Schematic illustration of the *stepped* resistance manipulation protocol in which the *active* resistance manipulation is repeated after waiting for some relaxation time  $t_{\text{Relax}}$ . During relaxation, we repeatedly measure the junction’s resistance with a period of  $t_{\text{Probe}}$  between measurements. (d) Measured resistance evolution during *stepped* manipulation in (c). The insert in (d) highlights the beginning of the third relaxation event.

As shown in figure 1(a), each manipulation experiment comprises  $N$  iterations, each consisting of  $M$  square-wave voltage pulses separated by a 100 ms blanking interval, followed by a resistance measurement. Unless otherwise noted, the pulse amplitude  $\pm V_a$  is set to 0.85 V, and we use  $M = 6$  pulses per iteration. The period of the square wave pulses is 200 ms, with symmetric positive and negative bias amplitudes. Both resistance manipulation and measurement are performed using a source-measurement unit mounted to a manual probe station in a four-wire configuration, as detailed in Appendix A.

The resistance is extracted from an I-V measurement in which the bias voltage  $V_m$  is swept linearly from  $-13$  mV to  $+13$  mV, while monitoring the sourced current. The junction resistance is obtained from a linear fit to the I-V data. The measurement period is intentionally set to an integer multiple of  $\frac{1}{50 \text{ Hz}} = 20$  ms to suppress AC mains interference. The setup described above is used for all experiments in this work, except for the aging and dielectric breakdown characterizations reported in section 3.2 and Appendix G, respectively, which are instead performed using an automated probe station described in Appendix A.

Figure 1(b) shows the typical junction response during active manipulation. We observe three distinct regimes: (i) an initial decrease in resistance, denoted  $R_{\text{Drop}}$ ; (ii) the active manipulation phase, during which the resistance is intentionally increased to  $R_{\text{Active}}$ ; and (iii) a post-manipulation relaxation characterized by a rapid rise followed by a long-tailed saturation at  $R_{\text{Total}}$  after the manipulation is halted at time  $t_{\text{Stop}}$ . During this relaxation phase, the source-measurement unit remains connected to the junction to continuously monitor the resistance without applying manipulation pulses.

Active manipulation always carries the risk of breaking the junction, most commonly through the formation of a short-circuit across the junction. This breaking mechanism has been linked to the glass-like behavior in Al-AlO<sub>x</sub>-Al Josephson junctions during annealing and relaxation [27]. This observation suggests that incorporating relaxation intervals between manipulation steps may reduce mechanical or structural strain. For this reason, we investigated *stepping* the active manipulation: we perform active resistance manipulation until a fixed increment relative to the initial resistance is reached, followed by a waiting time  $t_{\text{Relax}}$  during which the junction relaxes, after which the procedure is repeated. We refer to this protocol as *stepped* active manipulation. Figure 1(c) and (d) illustrate the waveform used for this process, and the resulting resistance changes, respectively. The results of our stepped manipulation experiments are presented in section 3.5.

## 2.2. Effect of resistance manipulation on qubit performance

The primary motivation of this work is to employ resistance manipulation for tuning qubit frequencies post-fabrication. We therefore investigate the impact of active manipulation on qubit decoherence and quality factor.

On the *high-dose* wafer, we fabricated two nominally identical devices,  $S_1$  and  $S_2$ ,

each containing eight fixed-frequency transmon qubits  $Q_1 - Q_8$ . Notably,  $S_1$  and  $S_2$  were fabricated adjacent to one another on the wafer. We performed two cryostat cooldowns using identical device mounting positions, cabling, and instrumentation. In the first cooldown,  $S_1$  served as a reference while  $S_2$  underwent active resistance manipulation. Prior to the second cooldown,  $S_1$  was manipulated, and  $S_2$  underwent a second manipulation process. During manipulation, the junction resistances increase, lowering the qubits' transition frequencies.

To assess qubit performance, we characterize decoherence metrics in section 3.6 by interleaving measurements of the energy relaxation time  $T_1$ , the Ramsey dephasing time  $T_2^*$ , and the Hahn-echoed dephasing time  $T_2^e$ . These measurements are repeated every 15 min over approximately one day per device per cooldown, with the distribution mean reported in table B2. Qubit quality factors are extracted from the measured  $T_1$  distributions.

### 3. Results

We now summarize the main results of this work. We first provide an overview of the Josephson junction samples and show that the measurement process itself does not induce resistance change, while confirming that natural aging depends on junction size. We demonstrate room-temperature active resistance manipulation and model how the resistance manipulation depends on the amplitude of the tuning signal. We compare the total resistance change to the actively induced resistance change, and show that a stepped manipulation protocol extends the accessible resistance range. Finally, we assess the impact of resistance manipulation on the decoherence and quality factors of transmon qubits.

#### 3.1. Josephson junction samples

Table 1 summarizes parameters of the Josephson junction samples studied in this work.  $R_W$  denotes the mean initial room-temperature resistances of the unmanipulated junctions. The electrode width  $\sqrt{A}$  is defined assuming junctions of square cross-sections, and  $R_W \cdot A$  is the corresponding resistance-area product. The oxidation parameters are the pressure  $p_{ox}$ , time  $t_{ox}$ , and dose  $D_{ox}$ , with  $D_{ox}$  being calculated using the empirical formula in [28]. *Age* specifies the time elapsed between fabrication and the first measurement, where  $t_0$  is defined as the time of the deposition of the second junction electrode, corresponding to the junction *birth time* [27].

#### 3.2. Aging

We characterized junction aging by monitoring the resistance spontaneously increasing under ambient laboratory conditions, with the aim of determining whether the measurement current or cadence of measurement influences aging.

**Table 1.** Summary of the five Josephson junction variants fabricated on three wafers of different oxidation doses, denoted as *low-dose*, *medium-dose*, and *high-dose*.

Sample	Low-dose 1	Low-dose 2	Medium-dose 1	High-dose 1	High-dose 2
$R_W$ [ $\Omega$ ]	11662	5513	11057	7840	6281
$\sqrt{A}$ [nm]	200	300	350	318	354
$R_W \cdot A$ [ $\text{n}\Omega \text{m}^2$ ]	0.47	0.50	1.35	0.79	0.79
Age [days]	> 182	> 359	> 364	> 102	> 102
$p_{ox}$ [mbar]	2	2	10	10	10
$t_{ox}$ [min]	20	20	60	150 <sup>‡</sup>	150 <sup>‡</sup>
$D_{ox}$ [ $\text{mbar}^{0.43} \cdot \text{min}^{0.65}$ ]	9.4	9.4	38.5	224.0	224.0

Measurements were performed at room temperature using an automatic probe station, described in [Appendix A](#). The junction geometries studied here differ from those stated in [table 1](#): the *low-dose* junctions feature electrode widths of 100 and 500 nm, and the *medium-dose* junctions feature widths of 200 and 600 nm, representing small and large devices, respectively.

To characterize and quantify resistance changes we define the resistance increase as

$$\Delta R(t) = \frac{R(t)}{R(0)} - 1 \quad , \quad (1)$$

where  $R(t)$  is the resistance measured at time  $t$ , with  $R(0)$  being the initial resistance. We express  $\Delta R(t)$  in units of % to enable comparison across junctions with different initial resistances and wafer origins. [Figure 2\(a\)](#) shows the natural  $\Delta R(t)$  evolution for varying measurement currents and measurement intervals; each trace corresponds to an individual junction tracked throughout the study. Similar to earlier work [\[29\]](#), we observe a significant increase of  $R(t)$  over a period of two weeks. We find no significant difference in aging behavior between frequently and infrequently measured samples, indicating that the resistance measurement do not measurably affect aging. Hence, we can assume that junctions can be measured safely without the junction changing its resistance beyond the extent it would have changed normally due to natural aging. While the data suggest slower aging for *medium-dose* junctions in comparison to *low-dose* junctions, a definitive comparison in this study is precluded by their later measurement start time, namely 19 days versus 2 days after deposition, respectively; and, additional post-deposition heating during the fabrication process for the *medium-dose* wafer, which is expected to reduce subsequent aging.

[Figure 2\(b\)](#) shows  $\Delta R(t)$  as a function of junction size. Each data point represents an average over measurements performed at bias currents of 25 nA, 50 nA, 100 nA, and 1  $\mu\text{A}$ ; for *low-dose* junctions, measurements at 10  $\mu\text{A}$  were also included. Each data

<sup>‡</sup> The oxidation time for the *high-dose* wafer is an estimate, due to a cleanroom power failure with no machine logs being saved for the actual time.

point is the average of all measurements acquired on the last measurement day for each junction size, corresponding to ages of 16 days for *low-dose* junctions and 32 days for *medium-dose* ones. Independent of oxidation dose, smaller junctions exhibit faster aging. This trend is consistent with previous reports of size-dependent resistance change in Nb-Al-AlO<sub>x</sub>-Nb junctions [12], although in that case the normal-state resistance was observed to decrease over time.

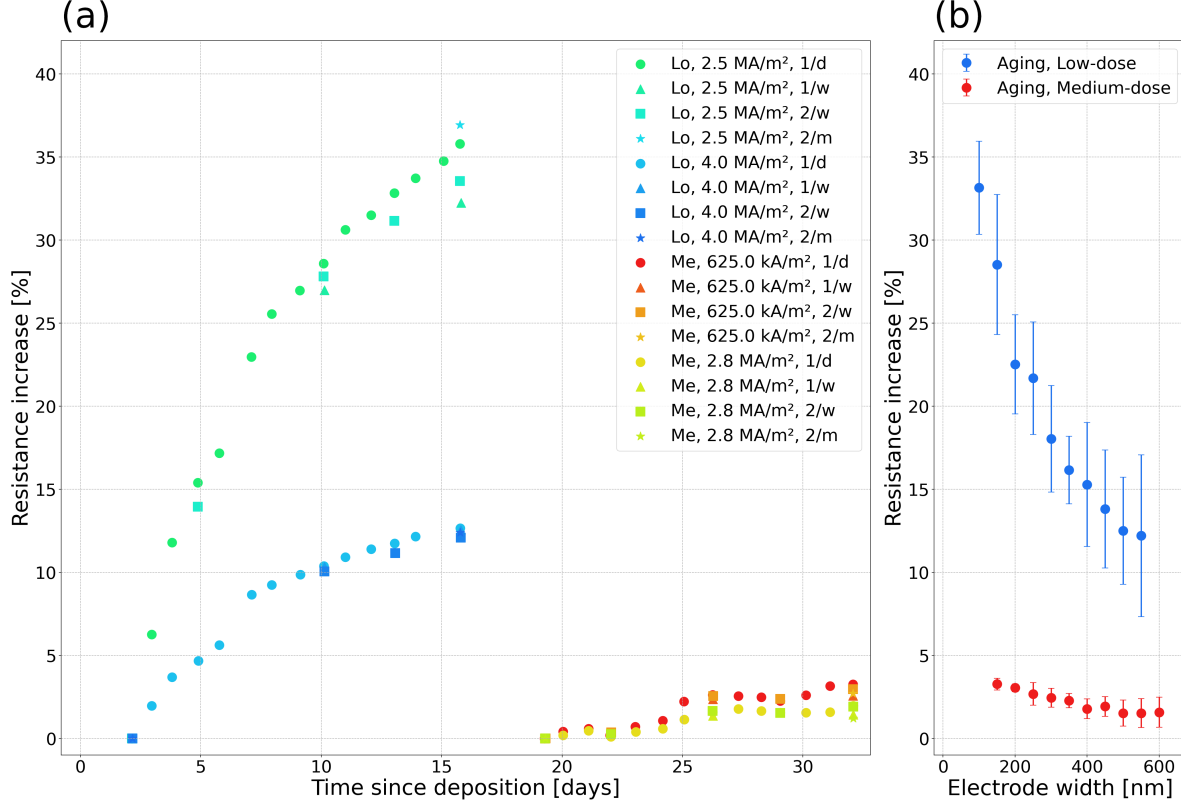


**Figure 2.** Natural aging of *low-dose* and *medium-dose* junctions of different sizes, denoted as *Lo* and *Me*, respectively. (a) Resistance increase as a function of time measured at different probe currents and measurement intervals; *1/d*: daily, *1/w*: weekly, *2/w*: biweekly, *2/m*: bimonthly. The legend indicates the measurement current density  $I/A$ . (b) Resistance increase of *low-dose* and *medium-dose* junctions as a function of junction electrode width. The *low-dose* data were measured 2 days after fabrication, and the *medium-dose* data after 19 days. When normalized to the earliest data point, the *medium-dose* junctions appear to age more slowly, likely reflecting them being 17 days older when measured.

Overall, our observations indicate (i) a spontaneous resistance increase of several tens of percent over a time scale of months, (ii) faster aging for smaller junctions, (iii) no measurable influence of the investigated measurement currents or measurement cadence on the aging process, and (iv) no conclusive difference in aging across oxidation doses within the constraints of this study.

### 3.3. Active manipulation

We manipulate the junction resistance by applying a train of voltage pulses, as shown in figure 1(a). Figures 3(a-e) show the actively induced  $\Delta R(t)$  as a function of time

for different pulse amplitudes  $V_a$ , measured across the five Josephson junctions variants listed in table 1. Across all devices, we find that an increasing  $V_a$  yields a higher rate of resistance change over time, with a maximum increase of 96.2% achieved in 5 min.

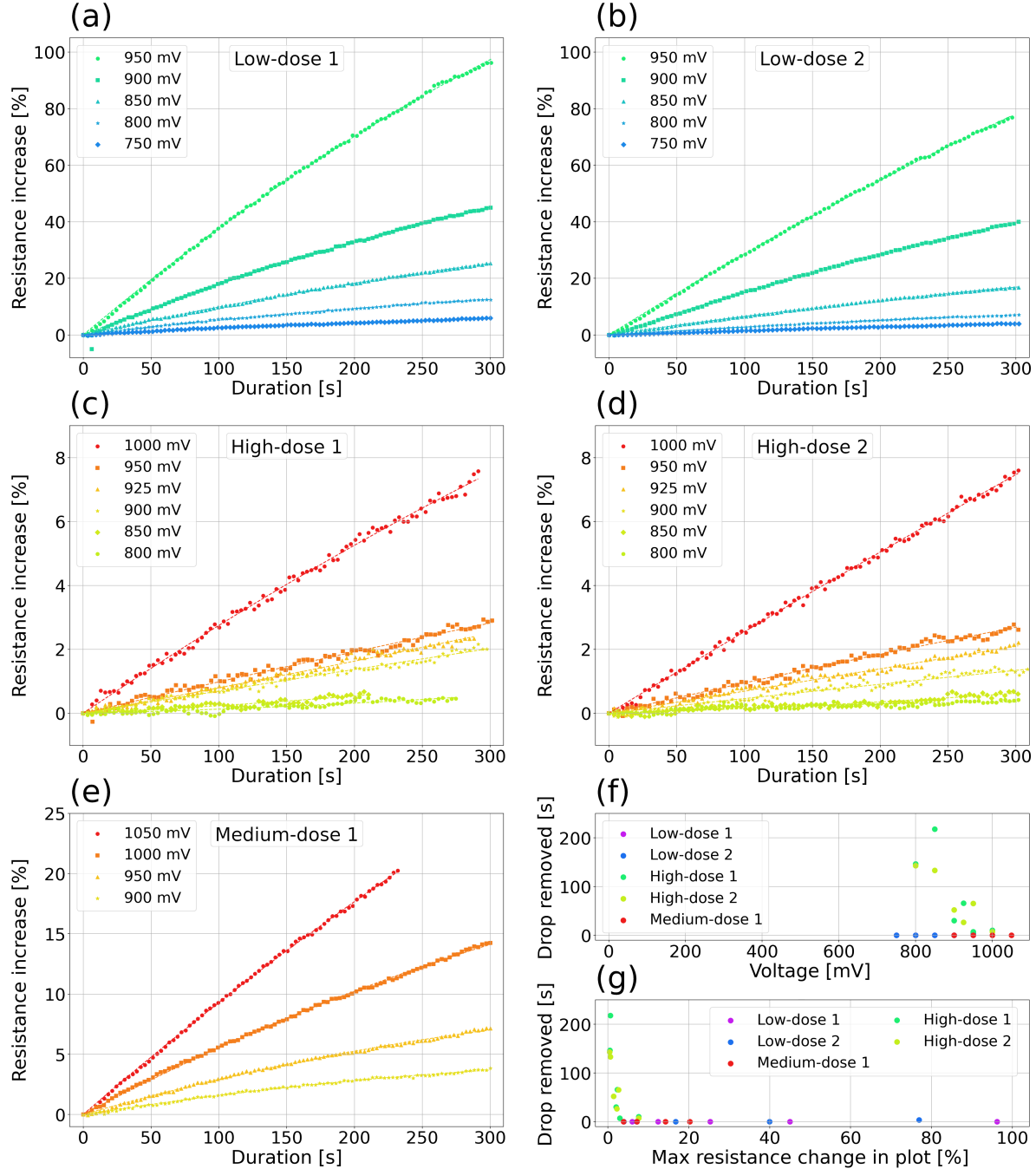


**Figure 3.** Resistance increase during active manipulation at multiple pulse amplitudes for (a) *low-dose 1*, (b) *low-dose 2*, (c) *high-dose 1*, (d) *high-dose 2*, and (e) *medium-dose 1* junctions. Manipulation at voltages exceeding the highest value shown in each panel resulted in junction failure. The time-dependent resistance change is dominated by a linear term  $\alpha(V)$  with a quadratic contribution  $\beta(V)$ , as defined in equation (2). (f) and (g) show the duration of the manually excluded initial resistance drop for each device set in (a-e), as a function of the manipulation voltage (f) and the maximum resistance change (g).

We fit the active resistance manipulation to a second-order polynomial equation

$$\Delta R(t) = \alpha(V) \cdot t + \beta(V) \cdot t^2 \quad , \quad (2)$$

where  $\alpha(V)$  and  $\beta(V)$  quantify the linear and quadratic time dependencies, respectively. The second-order polynomial was chosen empirically based on a comparison between four different candidate models, discussed in [Appendix D](#). The fit is restricted to the active manipulation regime shown in figure 1(b); prior to fitting, we remove the initial resistance drop, as illustrated in figures 3(f, g) and discussed further in [Appendix D.1](#).

Figure 4 shows the parameters obtained from fitting the data in figures 3(a-e) with equation (2). Figure 4(a) shows the linear coefficient  $\alpha(V)$  as a function of the manipulation pulse amplitude for the different samples. We find that  $\alpha(V)$  exhibits an exponential dependence on voltage, which we model as

$$\alpha(V) = \alpha_0 \cdot e^{V/V_0} \quad , \quad (3)$$

where  $V_0$  is the characteristic voltage corresponding to an  $e$ -fold increase in  $\alpha(V)$ , with  $\alpha_0$  being a prefactor modifying the voltage sensitivity. The extracted parameters are listed in table 2; increasing the pulse amplitude by approximately 200 mV results in at least an order-of-magnitude increase in the resistance-change rate for the *low-dose* and *high-dose* junctions, whereas the *medium-dose* junctions exhibit a more modest increase of about a factor of two over the measured range. Figure 4(a) also shows that samples from the same wafer cluster according to their resistance-area product  $R_W \cdot A$ , rather than junction area. This observation is consistent with previous reports indicating that electrical tuning exhibits only weak dependence on junction area [22]. Furthermore, the *medium-dose* manipulation results show that the resistance-area product alone is not sufficient for predicting the exponential voltage dependence, since the resistance-area product deviates from the trend held otherwise, where a higher resistance-area product equates to a sample showing a weaker response to increased manipulation amplitude. As seen in table 2, the prefactor  $\alpha_0$  spans over three orders of magnitude across the junctions while the extracted characteristic voltage  $V_0$  lies in the range 55–91 mV. Interestingly, these values are higher but comparable to the thermal voltage at room temperature,  $V_T \equiv k_B T / e \approx 25$  mV, consistent with slow resistance changes due to aging at room temperature.

**Table 2.** Parameters  $\alpha_0$  and  $V_0$  as extracted by fitting the data in figure 4(a). The % denotes the resistance increase percentage.

	Low-dose 1	Low-dose 2	Medium-dose 1	High-dose 1	High-dose 2
$\alpha_0$ [ $10^{-9}$ %/s]	824(351)	420(271)	1002(531)	0.79(119)	0.37(37)
$V_0$ [mV]	72.5(24)	70.4(34)	91.4(43)	57.5(50)	55.3(31)

Figure 4(b) shows the quadratic coefficient  $\beta(V)$  extracted from equation (2). The values of  $\beta(V)$  are predominantly negative, consistent with a decreasing rate of resistance

change over time; occasional positive values are close to zero and are attributed to fitting uncertainty. Since the quadratic term ultimately dominates at long times, we estimate the crossover time at which  $\beta(V)t^2$  surpasses  $\alpha(V)t$ . Across all junctions in figure 4, this time has a median of 26 min and a mean of 50 min, meaning that  $\alpha(V)$  remains the dominant source of resistance increase for the timescales observed in this study. The observation also implies the existence of a time where the resistance stops changing, assuming a hypothetical junction that survives active resistance manipulation for dozens of minutes.

Figures 4(c-e) compare  $\alpha(V)$  and  $\beta(V)$ , and weakly suggest an anticorrelation between the two parameters, with larger  $\alpha(V)$  accompanied by more negative  $\beta(V)$ . Physically, this trend implies that faster resistance changes are associated with more rapid deceleration of the tuning process: if a junction changes its resistance faster than before, then it would stop changing its resistance sooner. However, the limited data set precludes a statistically significant quantification of this relationship.

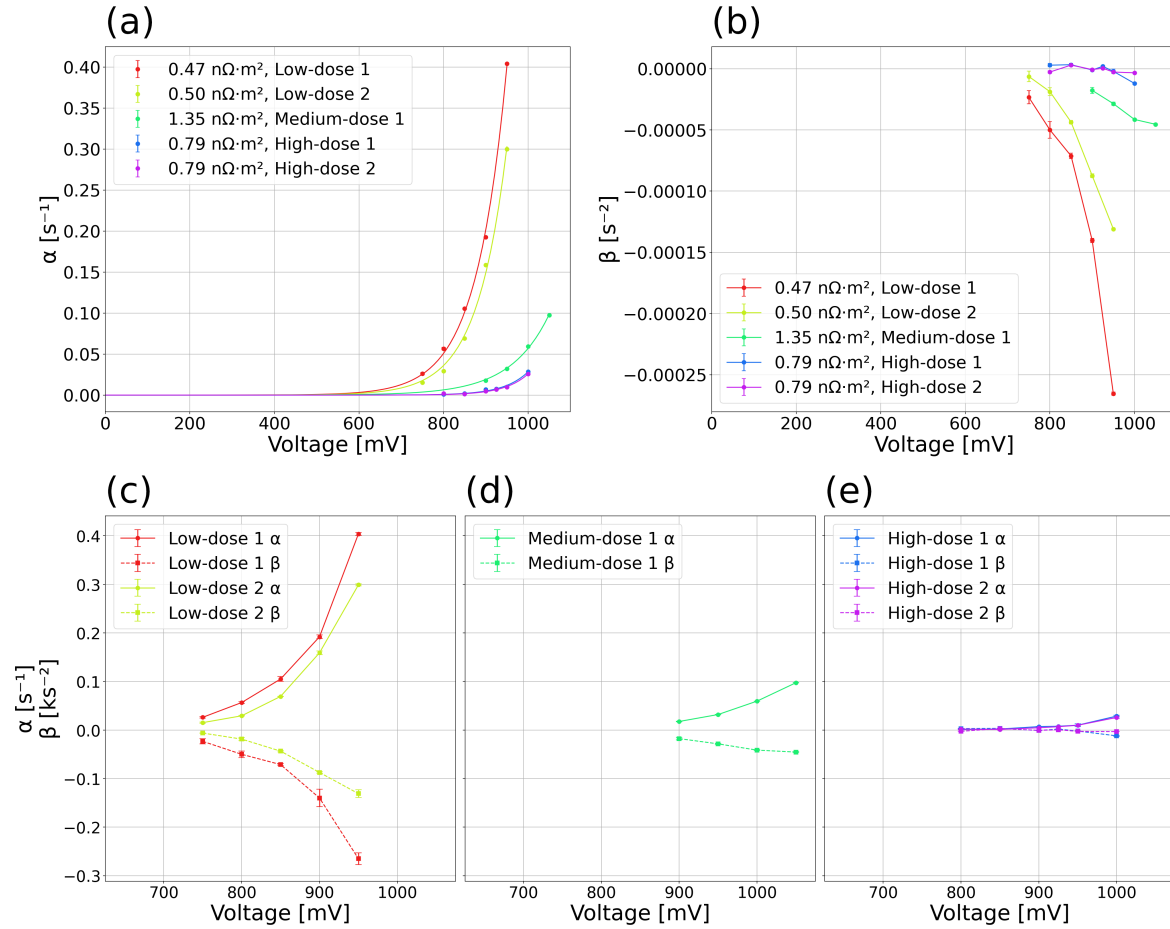


**Figure 4.** Extracted parameters (a)  $\alpha(V)$  and (b)  $\beta(V)$  obtained by fitting equation (2) to the resistance traces in figure 3. Panels (c-e) compare the voltage dependence of  $\alpha(V)$  and  $\beta(V)$ . The linear coefficient  $\alpha(V)$  exhibits an exponential dependence on voltage. The resistance-area product  $R_W A$  [nΩ m<sup>2</sup>] for the five junction variants is indicated in the legends of (a) and (b).

*3.3.1. The initial drop in resistance* As was shown in figure 1(b), we observe an initial decrease in resistance at the onset of active manipulation, consistent with previous reports [30]. The duration and magnitude of this drop are sample-dependent. In aged *low-dose* and *medium-dose* junctions, the effect is typically weak and limited to one or two data points, as shown in figure 3(f-g). In contrast, aged *high-dose* junctions exhibit a pronounced and extended resistance drop under comparable manipulation conditions. Performing the stepped active manipulation experiment outlined in section 2.1 also amplifies the initial resistance drop between iterations of the experiment, shown in figure D1.

### *3.4. Relaxation dependence on active manipulation*

Figure 1(b) shows that the junction has increased its resistance by  $R_{\text{Active}}$  when active manipulation ceases at a time  $t_{\text{Stop}}$ ; however, the junction's resistance continues to increase due to a relaxation mechanism, approaching a value  $R_{\text{Total}}$ . This relaxation follows a logarithmic time dependence and therefore lacks a well-defined asymptote; here, we define  $R_{\text{Total}} = R(t_{\text{Stop}} + 30 \text{ min})$ .

It has been reported that, when the active manipulation is stopped, the relaxation mechanism adds a fixed fraction of the initial resistance independently of how much the resistance was increased during active manipulation [30]. Under this observation, a plot of the total resistance increase as a function of the active resistance increase should yield a linear relation with unit slope and a finite offset. The offset quantifies the resistance added during relaxation at time  $t$ ,  $R_{\text{Total}} - R_{\text{Active}}$ . To test this behavior across different junction variants, we performed active manipulation to varying values for  $R_{\text{Active}}$ , measured the corresponding  $R_{\text{Total}}$ , and made a linear fit to the data.

Figure 5 shows the total resistance change  $\Delta R_{\text{Total}}$  as a function of the active increase  $\Delta R_{\text{Active}}$  for the (a) *low-dose 1*, (b) *medium-dose 1*, (c) *high-dose 1* and (d) *high-dose 2* junctions. The *high-dose* samples reproduce the previously reported behavior, with fitted slopes of  $1.00 \pm 0.01$  and  $1.04 \pm 0.04$ , for *high-dose 1* and 2, respectively. In contrast, *low-dose 1* and *medium-dose 1* exhibit larger slopes of  $1.13 \pm 0.01$  and  $1.08 \pm 0.02$ , respectively, indicating manipulation-dependent relaxation. We attribute these slope deviations to physical effects rather than systematic error, given the goodness of fit, low scatter, and the identical measurement protocol yielding unit slopes for the high-dose devices. Moreover, the fitted offsets differ across all samples, suggesting that relaxation is governed by intrinsic material properties.

As shown in figure 1(b), the resistance increase due to relaxation is not instantaneous. We therefore examined how the slope and offset parameters extracted from the linear fit between  $\Delta R_{\text{Total}}$  and  $\Delta R_{\text{Active}}$  evolve with the time elapsed after manipulation. This analysis was performed on the *low-dose 1* junctions, for which the largest data set was available. The results are reported in figure 6, and show that neither the slope nor the offset parameter stabilizes within 24 h. We fit their time dependence

empirically to a logarithmic growth function,

$$y(t) = a + b \cdot \ln(1 + t/\tau) \quad . \quad (4)$$

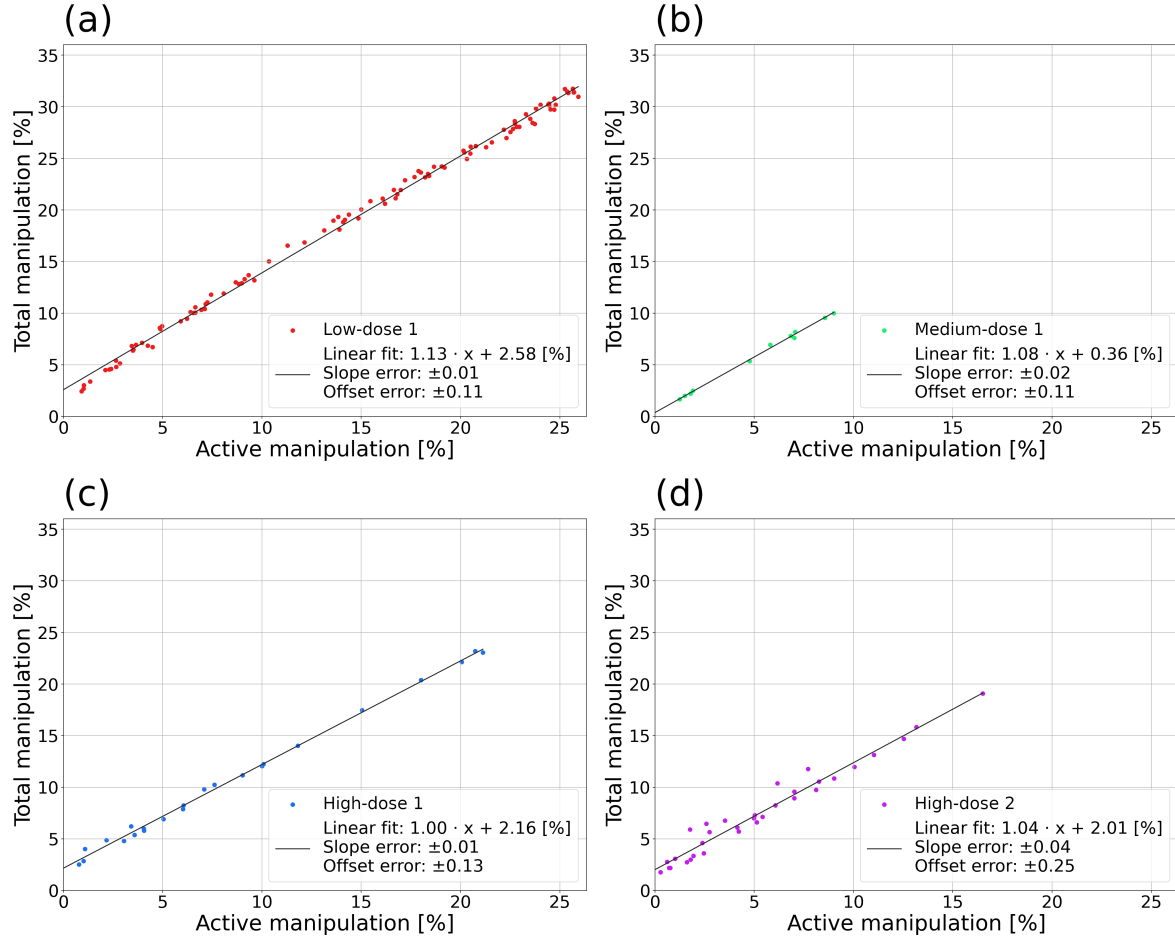
The logarithmic model was selected over a power-law fit, following a comparison reported in [Appendix E](#). The extracted fit parameters are shown in the legends.

Figure 6(a) shows how the linear fit slope  $\Delta R_{\text{Total}}/\Delta R_{\text{Active}}$  changes as a function of the time after manipulation is halted. We find that, in addition to the fixed relaxation offset observed independently of the magnitude of active manipulation, the relaxation process contributes with approximately one quarter of  $\Delta R_{\text{Active}}$  to  $\Delta R_{\text{Total}}$ . This result demonstrates that the relaxation is not always independent of the active manipulation. The amount of resistance increase gained during relaxation, due to the amount of active resistance manipulation made, is comparable in magnitude to the frequency tolerances required for tuning quantum processors. Figure 6(b) shows that resistance gained from relaxation regardless of the active manipulation, is  $3.29 \pm 0.19\%$ . The uncertainty of  $\pm 0.19\%$  is particularly relevant for qubit frequency targeting: as estimated in [Appendix C.1](#), this uncertainty sets a lower bound of 11.3 MHz on the achievable qubit frequency precision, about five times better than the regular fabrication precision. These results have direct practical implications for post-fabrication tuning: both the slope and offset of the relaxation process must be characterized to achieve accurate electrical tuning, requiring multi-day monitoring of statistically significant ensembles of sacrificial junctions.

### 3.5. Stepped active manipulation

We now demonstrate that stepped active manipulation can increase the junction resistance beyond the 96% achieved with regular active manipulation. The pulse sequence for the stepped scheme is shown in figure 1(c). Figure 7 presents the resistance evolution of a *low-dose 1* junction, aged 348 days at the time of measurement, as it is subjected to successive manipulation steps. Using this protocol, we increase the junction resistance by 269.5%, which, to our knowledge, is the largest resistance change reported for an individually targeted Josephson junction, corresponding to a transmon qubit shifting its frequency by  $\Delta f = -1964$  MHz. Upon further stepping, the junction ultimately fails during the initial resistance drop of the final manipulation step. We observe that the rate of resistance increase decreases with each successive step. At the same time, the magnitude of the initial resistance drop increases between steps, as shown in figure D1, to which we are unable to offer an explanation at this time.

Figure 8(a) shows the relaxation response normalized to the initial resistance at the beginning of the experiment  $R(t=0)$ , where each trace corresponds to the relaxation phase of a single manipulation step in figure 7. All steps exhibit similar relaxation dynamics, following an approximately logarithmic time dependence. The main difference between steps is that the relaxation traces are progressively shifting towards higher resistance values with each successive manipulation step. Figure 8(b) shows the junction's resistance increase during each relaxation phase, measured at the



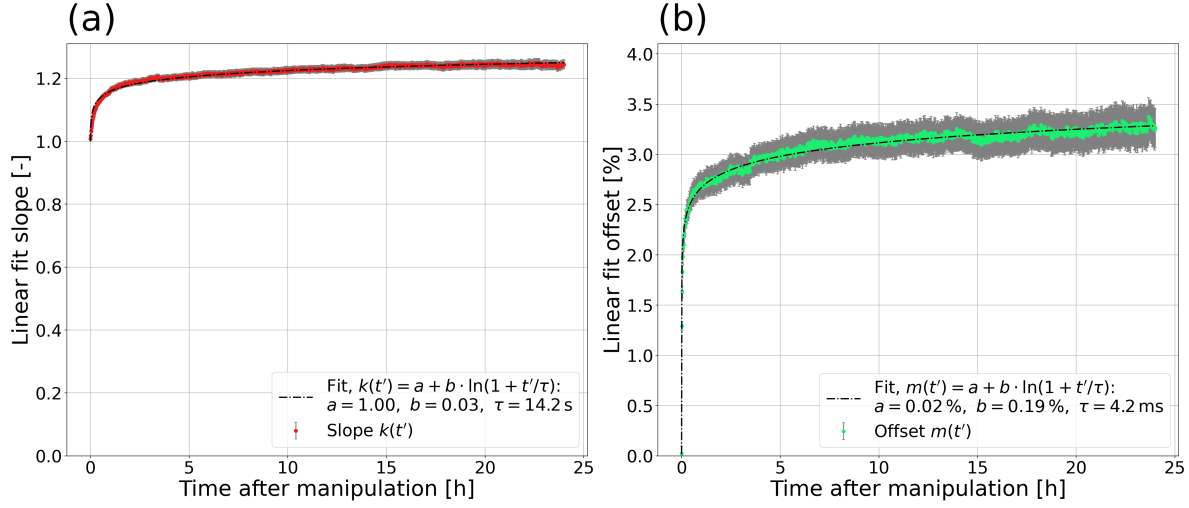
**Figure 5.** Linear fit of the *total* resistance manipulation as a function of the *active* resistance manipulation for (a) *low-dose 1*, (b) *medium-dose 1*, (c) *high-dose 1*, and (d) *high-dose 2* junctions. The *total* manipulation is evaluated 30 min after *active* manipulation ended; the vertical axes show  $R(t_{\text{stop}} + 30 \text{ min})/R(0) - 1$ . A slope of unity indicates that the relaxation contributes a fixed resistance increase offset independent of the actively induced resistance change.

30 min and 180 min markers in figure 8(a) as a function of time since the start of the stepped manipulation. The data reveal that the speed of the resistance increase grows with successive steps, suggesting that relaxation from earlier steps persists and contributes to subsequent relaxation phases.

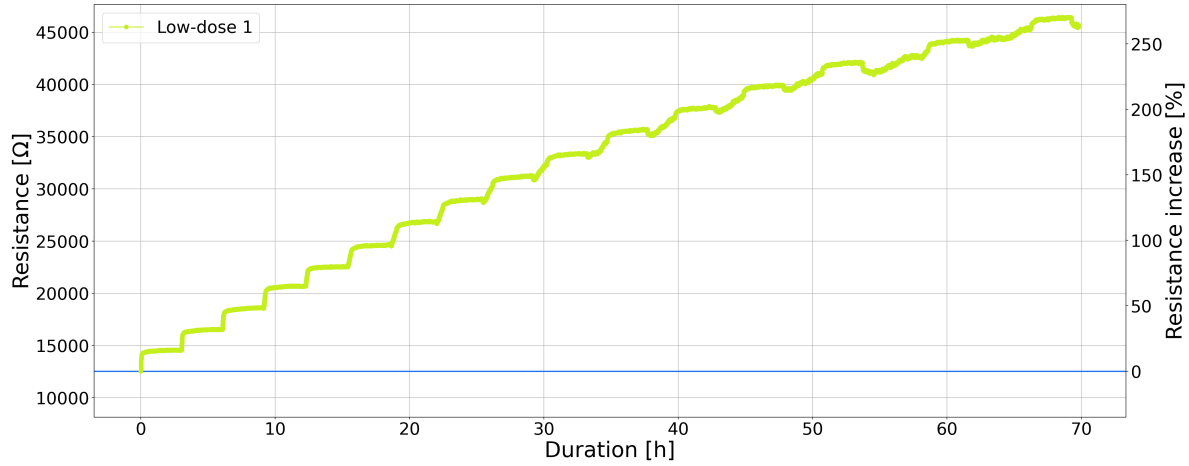
### 3.6. Decoherence factors and qubit quality

We study the effect of resistance manipulation on qubit coherence and quality factors using two devices,  $S_1$  and  $S_2$ , each containing eight fixed-frequency transmon qubits  $Q_{1..8}$ . During the first cooldown,  $S_1$  was measured as-fabricated, while  $S_2$  underwent resistance manipulation. In the second cooldown, both devices were manipulated, producing a “single-tuned”  $S_1$  and a “double-tuned”  $S_2$ .

The qubit quality factors are calculated as  $Q = 2\pi f_{01} \cdot T_1$  where  $f_{01}$  is the qubit frequency, and  $T_1$  its energy relaxation time measured during the two cooldowns. The measured  $f_{01}$ ,  $T_1$  and calculated  $Q$  values are reported in tables B1 and B2.



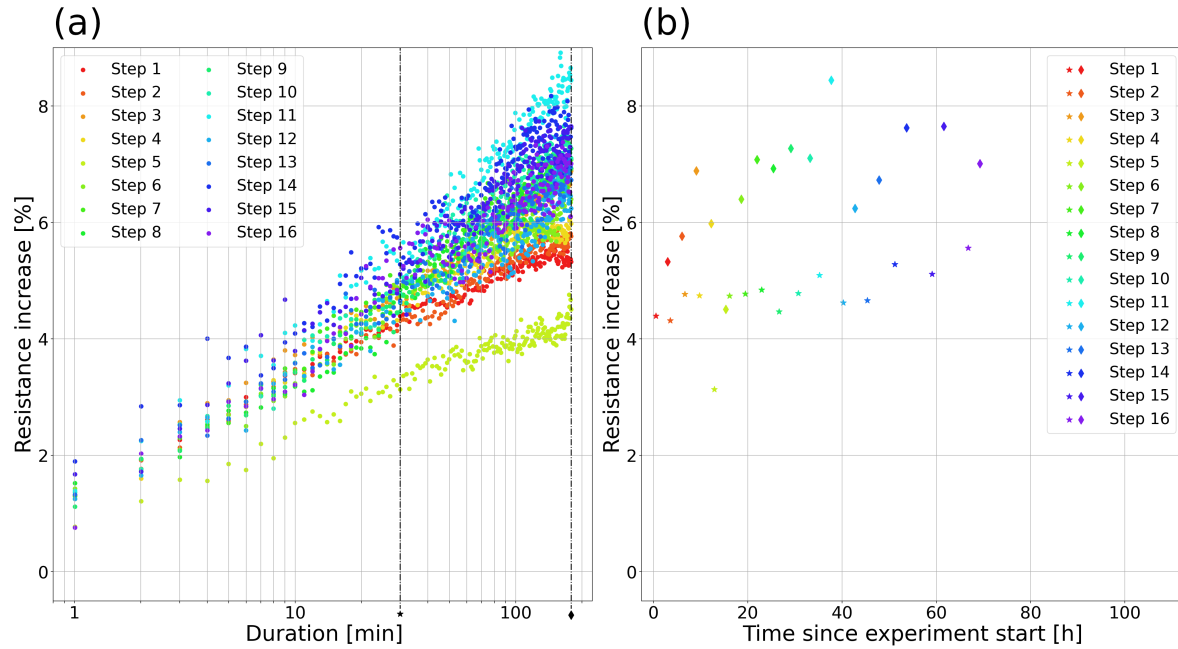
**Figure 6.** Time dependence of the slope (a) and offset (b) extracted from linear fits of total versus active resistance manipulation. An example of the  $t' = 30$  min fit is shown in figure 5(a).



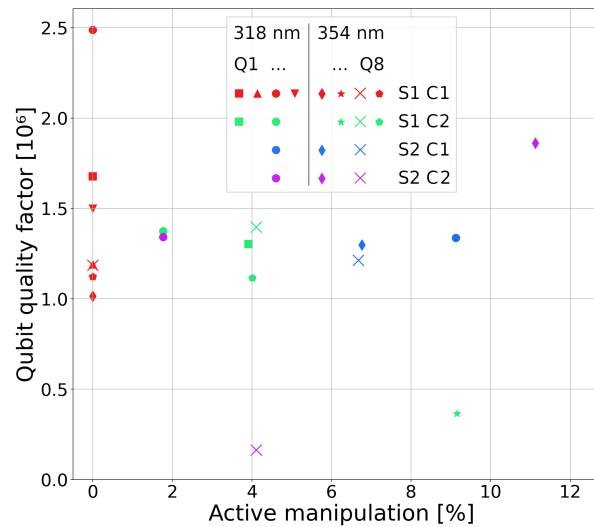
**Figure 7.** Stepped active manipulation of a 200 nm *low-dose* junction. Each step consists of an active resistance manipulation sequence that increases the junction resistance by  $+0.10 \cdot R(0)$ , followed by a 3 h relaxation period. The steps are repeated until junction failure, achieving a resistance change of  $\Delta R = +270\%$ . Using equation (C.4), this corresponds to a transmon frequency shift of  $\Delta f = -1964$  MHz.

Figure 9(a) shows qubit quality factors as a function of the resistance manipulation applied prior to two cooldowns, denoted  $C1$  and  $C2$ , respectively. Red symbols indicate the unmanipulated reference sample  $S_1$  while green symbols show  $S_1$  after a single manipulation step. Blue symbols correspond to the nominally identical sample  $S_2$ , manipulated once before  $C1$ , and purple symbols indicate  $S_2$  after a second manipulation prior to  $C2$ . We find that a single round of resistance manipulation preserves qubit performance, with  $Q$  values between 1 and 1.5 million, comparable to our previously reported devices [6]. Data following two manipulation rounds are inconclusive, with  $Q_5$  increasing in quality factor after major additional tuning, and  $Q_7$  decreasing in quality factor after minor additional tuning.

While resistance manipulation was successfully performed on most qubits, a fraction



**Figure 8.** Analysis of relaxation during the stepped active manipulation in figure 7. (a) Lin-log<sub>10</sub> plot of the relaxation after each step, normalized to  $R(0)$ . The relaxation traces mainly follow the same logarithmic time dependence as the first step, indicating repeated activation of the same relaxation process rather than a new one from a different resistance baseline. (b) Resistance increase evaluated at the 30 min and 180 min markers indicated in (a) as dashed vertical lines, shown as stars and diamonds, respectively. The increasing slope across steps indicates a growing relaxation rate with successive manipulations, suggesting ongoing relaxation from previous steps accumulates.



**Figure 9.** Qubit quality factor as a function of the active resistance manipulation. Each symbol shape denotes the same qubit across measurements. With a few exceptions, the qubit quality factors lie between  $1 \cdot 10^6$  and  $1.5 \cdot 10^6$  for one round of manipulation, comparable to those obtained with our standard fabrication process.

broke during the procedure. Electrostatic discharge (ESD) is unlikely the cause, as manipulation was initiated and sustained on all qubits for some time. Notably, failures occurred predominantly early in the process, with approximately half of the failures occurring within the first 6 min. We attribute the elevated failure rate primarily to

fabrication issues in the *high-dose* wafer. This wafer was produced using a newly commissioned evaporator for which the fabrication process had not yet been optimized; subsequent analysis revealed a less uniform deposition rate compared to other wafers studied here. Additional dielectric breakdown data for junctions from this wafer are presented in [Appendix G](#). Further work is needed to distinguish whether failures stem from the manipulation protocol or wafer-specific defects.

#### 4. Discussion and conclusion

In conclusion, we demonstrate a feasible method for manipulating the resistance of Josephson junctions. By studying multiple junction variants differing in size and oxidation dose, we confirm that natural aging is junction-size dependent, with smaller junctions aging more, and that resistance measurements performed at intervals ranging from daily to bimonthly do not measurably affect aging. We confirm earlier reports that the junction resistance can be actively increased at room temperature using electrical voltage pulses [31]. We find that the induced resistance increase follows a second-order time dependence dominated by its linear rate by two orders of magnitude. Crucially, we find that the linear rate depends exponentially on pulse amplitude, increasing by a factor of  $e$  for every additional 55–91 mV depending on the sample. Our data show that the resistance-area product alone does not predict the voltage dependence of the rate of resistance change, with one dataset disrupting an otherwise clear negative relationship.

Contrary to previous observations [30], the resistance increase observed after relaxation is not always a fixed fraction of the initial junction resistance. We find that this post-relaxation resistance change can increase with the amount of active manipulation made. During relaxation, the amount of resistance change gained from active manipulation, and gained passively from the relaxation process, both scale linearly with the initial resistance. We show that relaxation has a logarithmic time dependence regardless of the active manipulation, indicating that a manipulated sample at room-temperature requires monitoring over several hours to reliably extract relaxation parameters. The resulting uncertainty limits the achievable frequency precision of electrical tuning, which we estimate to be at least 11.3 MHz, and can possibly be reduced with greater control of the relaxation mechanism. We introduce a stepped active manipulation scheme that extends the accessible resistance range, achieving a total increase of up to 270% for an aged 12.5 k $\Omega$  junction at room temperature, the largest targeted resistance manipulation reported to date. We find that repeated steps amplify the initial resistance drop, an effect to which we currently offer no conclusive explanation. Moreover, repeated resistance manipulation steps leave cumulative effects in subsequent relaxation phases: the resistance increase measured at a fixed time after each relaxation onset, shows yet a gradual increase as the stepped manipulation experiment progresses. Finally, we show that performing resistance manipulation on qubits does not affect their performances, preserving quality factors above 1 million that are comparable to our standard fabrication outcomes. We do not observe any systematic dependence of

qubit quality factors on the manipulation process.

As superconducting quantum processors continue to scale, techniques enabling rapid, selective post-fabrication correction become increasingly critical. Electrical tuning provides a promising route, and this work clarifies both its capabilities and its practical limitations.

#### *4.1. Open questions and future experiments*

Multiple open questions remain that warrant further investigation. Future work should clarify how resistance manipulation affects junction parameters most relevant for qubit frequency targeting, namely the superconducting gap  $\Delta_g(T)$ , the charging energy  $E_C$ , and the room-temperature to cryogenic resistance ratio  $R/R_N$ , discussed in [Appendix C](#).

While we find an exponential dependence of the junction resistance on voltage amplitude, systematic studies of other waveform parameters, such as pulse duration, asymmetry, bandwidth-induced overshoot, and shape, are warranted. Complementary studies of dielectric properties before and after tuning, including breakdown voltage measurements, would provide insight into possible dielectric modifications induced by manipulation.

To assess contemporary speculations on whether the resistance manipulation is related to Cabrera-Mott oxidation, one could carefully increase the resistance until it plateaus, and subsequently apply a higher pulse amplitude to test whether resistance manipulation resumes. Theory suggests [32] that the resistance change would stagnate once an oxide film grows to a thickness where the electric field across it becomes too weak to sustain further growth; a revived resistance increase would suggest an oxide growth driven by an electric-field intensity. Similarly, the physical origin of the initial resistance drop remains unclear; the stepped active manipulation introduced here offers a promising route to isolating this effect as the drop increases with step count. Finally, extrinsic factors such as junction age and area should be disentangled by comparing relaxation slopes and offsets across same-wafer devices differing only in these parameters.

#### **Data availability statement**

The data that support the findings of this study are openly available at the following URL/DOI: <https://doi.org/10.5281/zenodo.17817324> [33].

#### **Acknowledgments**

For additional insights assisting this work, we thank Daryoush Shiri for his expertise in superconductivity and Anuj Aggarwal for discussions on quantum device design. We thank William Oliver at MIT for valuable insights and discussions regarding the possible physical mechanism behind electrical tuning and its similarities to natural aging. We thank Jürgen Lisenfeld at KIT for helpful discussions on electrical tuning and for

suggesting the experiment where a Josephson junction is rapidly submerged in liquid nitrogen during relaxation, which we present in the appendix.

We acknowledge financial support from the Knut and Alice Wallenberg Foundation (KAW) through the Wallenberg Center for Quantum Technology (WACQT), and in part from the EU Flagship on Quantum Technology under project HORIZON-CL4-2022-QUANTUM-01-SGA grant 101113946 OpenSuperQPlus100. The devices were fabricated at the Myfab Chalmers Nanofabrication Laboratory.

### **Conflict of interest**

A.N. and M.R. are board members and shareholders of Arkeon Technologies AB. The other authors declare no competing interests.

### **Appendix A. Experimental setup**

The room-temperature resistance manipulation and measurements were performed using a Keysight B2902B source-measurement unit, connected to a Keyfactor SimplePS manual probe station equipped with MPI MP40 probes and PT-W-S-2MIC tungsten needles. All measurements were conducted in an ESD-protected area, with an Ion Systems 6430 ionizer fan continuously directed at the sample being manipulated. Aging and dielectric breakdown measurements were carried out in an MPI TS2000-D automated probe station, using a Keithley 2612B System SourceMeter and a Keithley 3706A-S System Switch for sample multiplexing.

The microwave setup used for qubit characterization is illustrated in figure [A1](#). The samples were thermalized at the 10 mK stage of a Bluefors LD250 dilution refrigerator with highly-attenuated RF lines. Samples  $S_1$  and  $S_2$  share the same input/output readout line for all experiments, using coaxial microwave switches. Waveform generation and readout are handled using an IMP Presto-16-QC-DC AWG lock-in amplifier [[34](#), [35](#)]. The samples, illustrated in figure [A2](#), consist of 8 fixed-frequency transmon qubits whose readout resonators share a common feedline. The device parameters are given in table [B1](#).

### **Appendix B. Device parameters**

Table [B1](#) lists the measured and extracted parameters for samples  $S_1$  and  $S_2$  in the two cooldowns  $C1$  and  $C2$ . Table [B2](#) lists the acquired decoherence factors.

### **Appendix C. Relating resistance to qubit frequency**

The normal state resistance of a Josephson junction relates to the energy gap between the transmon qubit's  $|0\rangle$  and  $|1\rangle$  states through the Josephson energy [[24](#)], and ultimately through the Ambegaokar-Baratoff relation [[36](#), [37](#)]. For a transmon qubit with charging

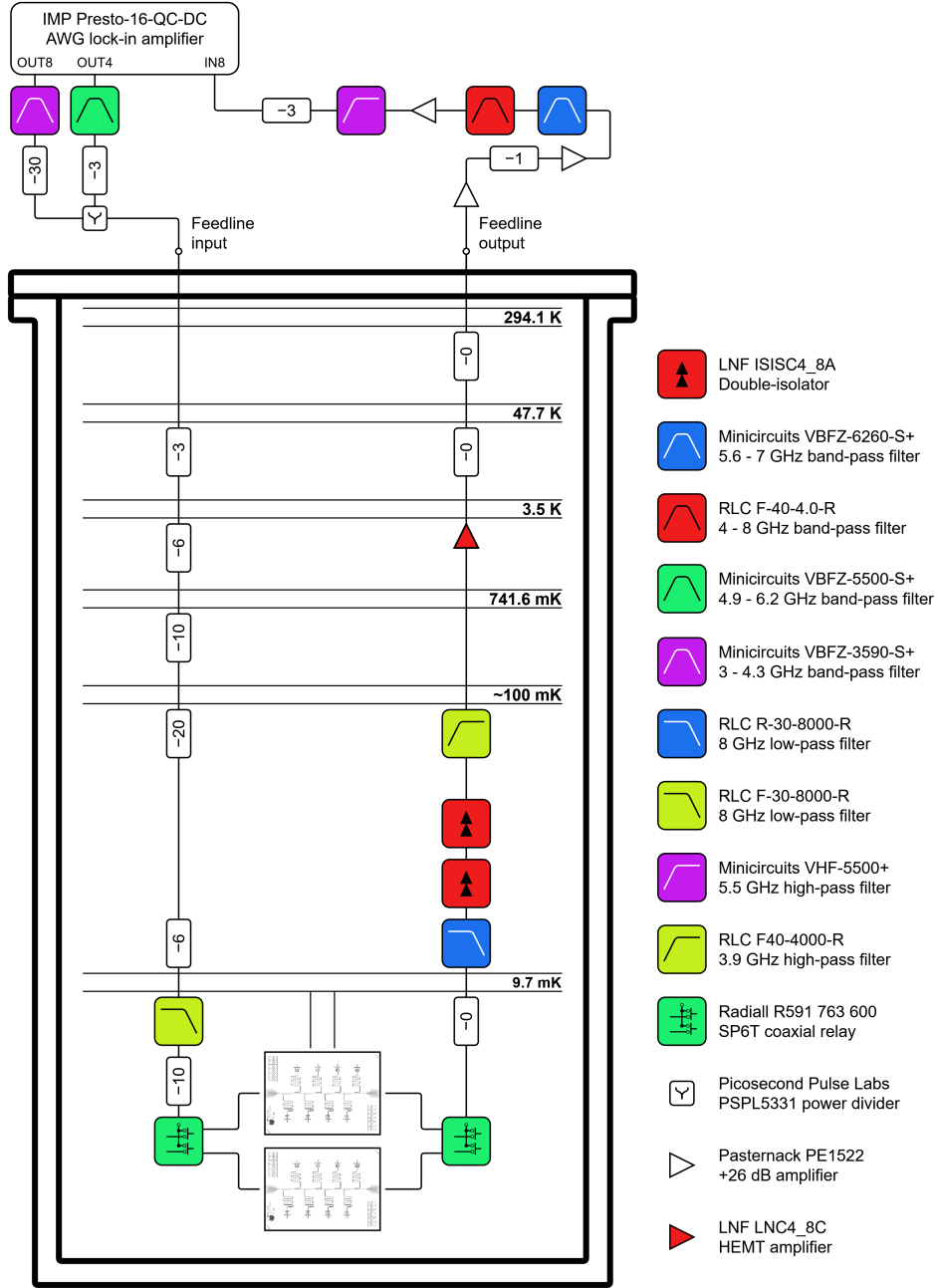


**Figure A1.** Full wiring diagram for the experimental setup. The numbers inside the attenuators indicate the attenuation in dB. The room-temperature attenuators before the feedline input optimize the operating range of the generated signals.

energy  $E_C = e^2/(2 \cdot C)$ , corresponding to the energy of a single Cooper pair stored in the transmon's capacitor [38], and Josephson energy  $E_J$ , the transition frequency  $f_{01}$  can be approximated [39] to

$$h f_{01} = \sqrt{8 E_J E_C} - E_C (1 + \xi 1/4 + \xi^2 21/128), \quad (\text{C.1})$$

where  $\xi = \sqrt{2 E_C/E_J}$ , and  $h$  is the Planck constant. The Josephson energy  $E_J$  is related

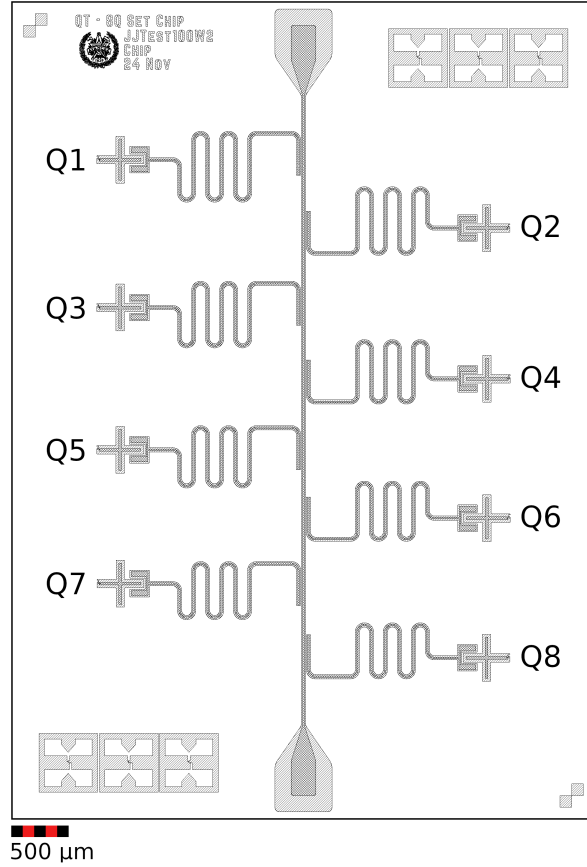


**Figure A2.** Quantum device chip layout. Qubits  $Q_1 - Q_4$  correspond to the *high-dose 1* junction variant in table 1, while  $Q_5 - Q_8$  correspond to *high-dose 2* junctions. The two samples  $S_1$  and  $S_2$  were fabricated adjacent to one another on the same wafer.

to the critical current  $I_C$  via

$$E_J = \frac{\Phi_0}{2\pi} I_C = \frac{\hbar}{2e} I_C \quad , \quad (\text{C.2})$$

where  $\Phi_0$  is the magnetic flux quantum and  $e$  the electron charge. The critical current  $I_C$  relates to the normal state resistance  $R_N$  of the junction through the Ambegaokar-Baratoff relation

$$I_C = \frac{\pi \Delta_g(T)}{2e R_N} \tanh\left(\frac{\Delta_g(T)}{2k_B T}\right) \quad , \quad (\text{C.3})$$

where  $\Delta_g(T)$  is the superconducting energy gap,  $k_B$  is the Boltzmann constant, and  $T$  is the superconductor temperature. For a non-manipulated *medium-dose* junction, we measured  $\Delta_g(T \approx 10 \text{ mK}) = 174.3 \text{ } \mu\text{eV}$ , yielding  $\tanh\left(\frac{\Delta_g(T)}{2k_B T}\right) \approx 1$  in equation (C.3). We note that our measured superconducting energy gap is close to the textbook number for bulk aluminum  $\Delta_g(T) \approx 178.2 \text{ } \mu\text{eV}$  [40], resulting in  $\frac{2\Delta_g(0.01)}{\alpha_{\text{BCS}} \cdot k_B} = T_c \approx 1.16 \text{ K}$ , where  $\alpha_{\text{BCS}} = 3.5$  is the ideal gap ratio [41]. For reference, the nominal film thicknesses of this junction are 39 nm for the bottom electrode, and 78 nm for the top electrode.

Substituting equation (C.3) into equation (C.2), and subsequently into equation (C.1), completes a relation between the normal state resistance  $R_N$  and the qubit

**Table B1.** Characteristic parameters of samples  $S_1$  and  $S_2$ , which underwent one and two cycles of resistance manipulations, respectively.  $C1$  and  $C2$  denote the two cryostat cooldowns.  $f_{\text{res},|0\rangle}$  is the resonator frequency when the corresponding qubit is in  $|0\rangle$ ,  $\kappa$  is the energy decay rate of the resonator,  $\eta$  is the transmon anharmonicity,  $f_{01}$  is the qubit's  $|0\rangle \rightarrow |1\rangle$  transition frequency, and  $2\chi$  is the dispersive shift.

$S_1$	$f_{\text{res}, 0\rangle}$ [GHz]	$\kappa/2\pi$ [kHz]	$\eta/2\pi$ [MHz]		$f_{01}$ [GHz]		$2\chi$ [kHz]		$Q$ [-]	
			C1	C2	C1	C2	C1	C2	C1	C2
			$Q_1$	5.9532	818		-214.4	4.8514	4.5518	-3108
$Q_2$	6.0659	707	-210.0		4.9853		-1764		1 190 290	
$Q_3$	6.1935	730		-222.2	4.1680	4.0851	-1024	-411	2 487 886	1 375 136
$Q_4$	6.3155	692	-210.3		4.9750		-1435		1 500 422	
$Q_5$	6.4513	767	-202.3		5.5673		-2887		1 014 434	
$Q_6$	6.5924	812	-204.8	-197.6	5.4177	4.9811	-1671	-899	1 123 330	365 889
$Q_7$	6.7446	924	-201.7	-207.2	5.3942	5.1232	-1434	-965	1 186 250	1 397 712
$Q_8$	6.8918	898	-203.2	-205.3	5.5847	5.2863	-1627	-1159	1 122 872	1 116 143
<hr/>										
$S_2$										
$Q_1$	5.9509	646	-212.7		4.7759		-1495		840 215	
$Q_2$	6.0668	647								
$Q_3$	6.1908	754	-216.8	-222.0	4.4353	4.2354	-778	-620	1 337 651	1 341 931
$Q_4$	6.3127	735								
$Q_5$	6.4554	777	-207.4		5.1634	4.8590	-1495	-2054	1 297 704	1 860 994
$Q_6$	6.5811	735								
$Q_7$	6.7419	815	-208.9		4.9492	4.8039	-857	-574	1 212 784	163 470
$Q_8$	6.8838	1011								

frequency  $f_{01}$ ,

$$hf_{01} = \sqrt{8E_C \frac{\hbar\pi\Delta_g(T)}{4e^2R_N}} - E_C \left( 1 + \frac{1}{4} \sqrt{\frac{2E_C}{\frac{\hbar\pi\Delta_g(T)}{4e^2R_N}}} + \frac{21}{128} \sqrt{\frac{2E_C}{\frac{\hbar\pi\Delta_g(T)}{4e^2R_N}}} \right). \quad (\text{C.4})$$

$R_N$  relates to the Josephson junction's resistance measured at room temperature. We use a fixed conversion rate  $R_N = R \cdot 1.1385$  based on previous measurements taken on a *low-dose* sample [9]. Hence, we can use equation (C.4) to estimate the change in qubit frequency given an induced change in  $R$ . We measure the junction's resistance from its I-V characteristics using a voltage sweep from  $-13$  mV to  $+13$  mV, a region where the junction is resistor-like [42], fitting the data to a purely linear model  $V = R \cdot I$  giving us a high coefficient of determination  $r^2 = 1.000(1)$ .

#### Appendix C.1. Tuning frequency precision from the relaxation offset error

In figure 6(b), the uncertainty in the relaxation fit offset relating  $R_{\text{Total}}$  to  $R_{\text{Active}}$ , is approximately  $\pm 0.19\%$ . This uncertainty directly translates into an imprecision in the

**Table B2.** Decoherence times for samples  $S_1$  and  $S_2$  across two cooldowns,  $C1$  and  $C2$ . Entries labeled  $n/a$  indicate data with uncertainties too large to report reliably, while blank entries correspond to qubits that failed.  $S_2$  was resistance-manipulated prior to  $C1$ , whereas both  $S_1$  and  $S_2$  underwent manipulation prior to  $C2$ .

		$T_{1, C1}$ [ $\mu$ s]	$T_{1, C2}$ [ $\mu$ s]	$T_{2, C1}^*$ [ $\mu$ s]	$T_{2, C2}^*$ [ $\mu$ s]	$T_{2, C1}^e$ [ $\mu$ s]	$T_{2, C2}^e$ [ $\mu$ s]
$S_1$	$Q_1$	$55 \pm 6$	$46 \pm 7$	$25 \pm 6$	$23 \pm 5$	n/a	$29 \pm 3$
	$Q_2$	$38 \pm 7$		$47 \pm 3$		$73 \pm 4$	
	$Q_3$	$95 \pm 17$	$54 \pm 12$	$34 \pm 16$	$17 \pm 4$	$65 \pm 7$	$62 \pm 8$
	$Q_4$	$48 \pm 10$		$49 \pm 13$		$72 \pm 5$	
	$Q_5$	$29 \pm 4$		$38 \pm 5$		$57 \pm 4$	
	$Q_6$	$33 \pm 2$	$12 \pm 1$	$19 \pm 7$	$4 \pm 1$	$56 \pm 5$	$21 \pm 1$
	$Q_7$	$35 \pm 5$	$43 \pm 8$	$9 \pm 1$	$40 \pm 6$	$57 \pm 7$	$52 \pm 6$
	$Q_8$	$32 \pm 3$	$34 \pm 7$	$37 \pm 4$	$37 \pm 7$	$53 \pm 6$	$44 \pm 6$
$S_2$	$Q_1$	$28 \pm 3$		$21 \pm 4$		$37 \pm 3$	
	$Q_2$						
	$Q_3$	$48 \pm 7$	$50 \pm 9$	$36 \pm 16$	$21 \pm 2$	$66 \pm 7$	$57 \pm 7$
	$Q_4$						
	$Q_5$	$40 \pm 3$	$61 \pm 11$	$33 \pm 5$	$14 \pm 10$	$61 \pm 4$	n/a
	$Q_6$						
	$Q_7$	$39 \pm 5$	$5 \pm 0.1$	$39 \pm 8$	$1 \pm 0.1$	$67 \pm 9$	n/a
	$Q_8$						

qubit frequency, which we estimate here.

We conservatively assume that the relaxation-offset uncertainty extracted from the *low-dose 1* junctions represents an equal or worse case for both *high-dose* variants used as qubit devices, for which we have experimental data. We further assume an energy gap  $\Delta_g(T \approx 10 \text{ mK}) = 174.3 \text{ } \mu\text{eV}$ , measured on a *medium-dose* junction, and use the room-temperature to normal-state resistance conversion  $R_N = R \cdot 1.1385$ , as described in the previous section. We base our estimate for frequency precision on the unmanipulated reference device's *high-dose 2* junctions, using qubits  $Q_5$ – $Q_8$  in table B1, which have a mean transition frequency  $f_{01} = 5.4910 \text{ GHz}$  and a mean anharmonicity  $\eta/2\pi = -203.0 \text{ MHz}$ . Using [39] with the same  $\xi$  from equation (C.1),  $E_C$  is given by

$$\frac{\eta}{2\pi} = -E_C - \frac{9}{16}(E_C \xi) - \frac{81}{128}(E_C \xi^2) - \frac{3645}{4096}(E_C \xi^3) - \frac{46899}{32768}(E_C \xi^4). \quad (\text{C.5})$$

Enforcing  $\eta/2\pi = -203.0 \text{ MHz}$  in equation (C.5) while simultaneously solving (C.4) to  $f_{01} = 5.4910 \text{ GHz}$ , creates a bound solution for  $R$ . Numerically, we find  $R$  to be  $5521.4 \Omega$ , resulting in  $E_J = 21.63 \text{ GHz}$  from equations (C.2) and (C.3), and  $E_C = 186.7 \text{ MHz}$  from equation (C.5).

We repeat this procedure for  $R \pm 0.19\%$ , which yields a frequency error of  $5496.6 - 5485.3 = 11.3 \text{ MHz}$ . We therefore assume that the uncertainty associated with

the relaxation offset alone imposes a best-case bound of approximately 11.3 MHz on the attainable frequency precision of electrical tuning, under the assumption considered here.

## Appendix D. Additional manipulation analysis with secondary trends

This section details additional analysis and observations used to refine the interpretation of resistance changes in our devices. We first address the removal of the initial resistance drop observed in figure 3, which is necessary for fitting the time-dependent resistance using equation (2). We then justify the use of a second order polynomial in equation (2) to model active resistance manipulation. Finally, we supplement figure 4 and table 2 with equivalent results in units of  $\Omega \text{s}^{-1}$  and  $\Omega \text{s}^{-2}$ .

### Appendix D.1. Resistance drop

The resistance drop is removed from the dataset prior to fitting equation (2). For completeness, the removed resistance drop for each fit is shown as a function of manipulation voltage in figure 3(f), and as a function of the maximum reported resistance increase in figure 3(g). We observe no clear dependence of the initial resistance drop on either resistance change or voltage range. The only systematic trend is that *high-dose* devices consistently exhibit a significantly larger drop than the *low-dose* and *medium-dose* devices.

Furthermore, we note that the resistance drop increases with each successive step in the stepped active manipulation experiments. Figure D1 shows  $R_{\text{Drop}}$  as a function of  $\Delta R(t)$  at the start of each manipulation step in figure 7. The initial drop deepens progressively with each step, before the behavior becomes chaotic. At present, we do not have a definitive explanation for this trend.

### Appendix D.2. Selecting a model for active resistance manipulation

We selected the polynomial model empirically by systematically comparing several candidate models for the fractional resistance change  $R(t)/R(0) - 1$ : a second-order polynomial, a third-order polynomial, an exponential, and a power law. Only the second- and third-order polynomials adequately captured the experimentally observed resistance evolution; their RMS errors are summarized in table D1. The mean difference shows that the performance of the third-order polynomial over the second-order polynomial is a few hundredths of percent better, at the cost of adding an additional degree of freedom into the model. We thus adopt the second-order polynomial as the simplest phenomenological model that represents the experimentally observed resistance increase over time, motivated by the fact that the model has fewer free variables at near-equal error.

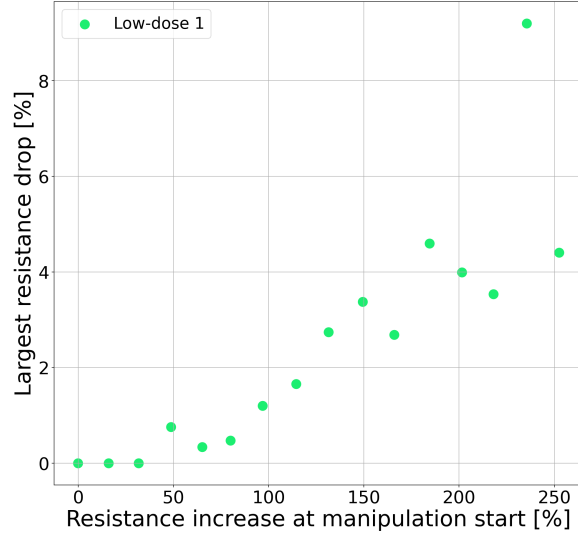


**Figure D1.** Initial resistance drop at each step during the stepped active manipulation in figure 7, as a function of the resistance increase. The drop magnitude increases with successive steps, after which the trend becomes irregular.

**Table D1.** RMS error comparison between the second-order polynomial fit and a third-order polynomial fit for each resistance manipulation fit in figure 3 in the same units as the figure, that is, % resistance increase.  $V_a$  denotes the manipulation voltage.

$V_a$ [mV]	750	800	850	900	925	950	1000	1050	
<b>Difference</b>									Mean
Low-dose 1	0.024	0.018	0.004	0.004		0.089			0.028
Low-dose 2	0.006	0.037	0.020	0.051		0.141			0.051
Medium-dose 1				0.0002		0.004	0.044	0.008	0.014
High-dose 1		0.003	0.006	0.003	0.004	0.005	0.00001		0.004
High-dose 2		0.003	0.003	0.0006	0.0003	0.004	0.0001		0.002
<b>2nd-order</b>									Mean
Low-dose 1	0.121	0.180	0.219	0.691		0.544			0.351
Low-dose 2	0.079	0.149	0.139	0.307		0.422			0.219
Medium-dose 1				0.078		0.092	0.123	0.129	0.105
High-dose 1		0.072	0.070	0.078	0.084	0.101	0.128		0.088
High-dose 2		0.066	0.067	0.088	0.083	0.086	0.095		0.081
<b>3rd-order</b>									Mean
Low-dose 1	0.097	0.162	0.214	0.686		0.455			0.323
Low-dose 2	0.072	0.112	0.119	0.256		0.281			0.170
Medium-dose 1				0.078		0.088	0.078	0.121	0.092
High-dose 1		0.069	0.064	0.075	0.080	0.097	0.128		0.085
High-dose 2		0.063	0.063	0.088	0.083	0.082	0.095		0.079

## Appendix D.3. Ohmic comparison of resistance change parameters

Tables D2 and D3 present the fit results for  $\alpha(V)$  and  $\beta(V)$ , multiplied by the respective  $R(0)$  of each fitted trace, to convert the fractional units into  $\Omega \text{ s}^{-1}$  and  $\Omega \text{ s}^{-2}$ , respectively. We denote these rescaled parameters as  $\alpha'$  and  $\beta'$ . Similarly, table D4 reports the resulting  $\alpha'_0$  in units of  $\Omega \text{ s}^{-1}$ . For comparison, the characteristic voltage  $V_0$  is also included and is identical its values in table 2.

**Table D2.** Extracted  $\alpha'$  and  $\beta'$  parameters for the *low-dose* devices.

	<b>Low- dose 1</b>	<b>Low- dose 1</b>	<b>Low- dose 2</b>	<b>Low- dose 2</b>
Voltage	$\alpha'$ [ $\Omega \text{ s}^{-1}$ ]	$\beta'$ [ $\text{m}\Omega \text{ s}^{-2}$ ]	$\alpha'$ [ $\Omega \text{ s}^{-1}$ ]	$\beta'$ [ $\text{m}\Omega \text{ s}^{-2}$ ]
750 mV	2.93(15)	-2.6(5)	0.80(5)	-0.328(23)
800 mV	6.42(18)	-5.7(8)	1.56(4)	-1.00(17)
850 mV	12.1(6)	-8.23(25)	3.920(17)	-2.46(8)
900 mV	22.6(5)	-16.5(21)	8.48(21)	-4.66(8)
950 mV	50.3(4)	-33.0(15)	17.96(12)	-7.9(5)

**Table D3.** Extracted  $\alpha'$  and  $\beta'$  parameters for the *medium-dose* and *high-dose* devices.

	<b>Medium- dose 1</b>	<b>Medium- dose 1</b>	<b>High- dose 1</b>	<b>High- dose 1</b>	<b>High- dose 2</b>	<b>High- dose 2</b>
Voltage	$\alpha'$ [ $\Omega \text{ s}^{-1}$ ]	$\beta'$ [ $\text{m}\Omega \text{ s}^{-2}$ ]	$\alpha'$ [ $\Omega \text{ s}^{-1}$ ]	$\beta'$ [ $\text{m}\Omega \text{ s}^{-2}$ ]	$\alpha'$ [ $\Omega \text{ s}^{-1}$ ]	$\beta'$ [ $\text{m}\Omega \text{ s}^{-2}$ ]
800 mV			0.0809(26)	0.238(11)	0.130(15)	-0.174(7)
850 mV			0.159(19)	0.259(8)	0.073(13)	0.185(6)
900 mV	1.99(5)	-2.00(27)	0.543(17)	-0.076(8)	0.255(11)	-0.035(4)
925 mV			0.602(15)	0.153(6)	0.446(5)	0.0266(13)
950 mV	3.46(3)	-3.09(12)	0.78(23)	-0.162(14)	0.632(10)	-0.173(5)
1000 mV	6.762(23)	-4.71(10)	2.28(16)	-0.95(6)	1.70(10)	-0.217(5)
1050 mV	10.449(21)	-4.87(9)				

**Table D4.** Fit parameter  $\alpha'_0$  and the corresponding characteristic voltage  $V_0$ . This voltage represents the additional voltage required for the linear rate of resistance change, to increase by a factor  $e$ .

	<b>Low- dose 1</b>	<b>Low- dose 2</b>	<b>Medium- dose 1</b>	<b>High- dose 1</b>	<b>High- dose 2</b>
$\alpha'_0$ [ $\mu\Omega \text{ s}^{-1}$ ]	98.2(23)	21.5(13)	108.4(33)	0.0650(5)	0.0253(5)
$V_0$ [mV]	72.5(24)	70.4(34)	91.4(43)	57.5(50)	55.3(31)

## Appendix E. Residual analysis between relaxation models

To characterize the relaxation growth, we compare the logarithmic model in equation (4) with a power-law description,

$$y(t) = a + c \cdot t^d. \quad (\text{E.1})$$

We evaluate the mean and variance of the residuals  $\Delta k$ ,  $\Delta m$  between the fitted curves and the measured data. For the logarithmic model, the mean residuals are  $\langle \Delta k \rangle = -1.42 \cdot 10^{-5}$  and  $\langle \Delta m \rangle = -8.59 \cdot 10^{-6}$ , with variances  $2.04 \cdot 10^{-5}$  and  $1.63 \cdot 10^{-3}$ , respectively. In contrast, the power-law model yields larger residuals, with mean values  $\langle \Delta k \rangle = -9.16 \cdot 10^{-5}$  and  $\langle \Delta m \rangle = -1.06 \cdot 10^{-4}$  and variances  $5.16 \cdot 10^{-5}$  and  $2.18 \cdot 10^{-3}$ . The consistently smaller residuals and variances indicate that the relaxation growth is better described by a logarithmic dependence than by a power law. In all fits, we enforced a minimum bound for  $a$  being 1 corresponding to  $R_{\text{Total}}(t_{\text{Stop}})/R_{\text{Active}}(t_{\text{Stop}}) = 1$ , as no relaxation has yet occurred at the stopping time.

## Appendix F. A thermally activated process

The term *electrical annealing* is commonly used to describe the resistance manipulation process studied in this work. However, the terminology *annealing* can be misleading, as there is strong evidence that the underlying physical process does not primarily rely on heating the junction to conventional annealing temperatures. Instead, the experimental picture that emerges is that electrical tuning is fundamentally a thermally activated process, in which the electric field plays an essential role.

To demonstrate how the manipulation process is influenced by temperature, we performed an ad-hoc experiment. We performed resistance manipulation at room temperature, after which the junction was allowed to relax while submerged in liquid nitrogen. The experiments were carried out in an aluminum enclosure, surrounded by a styrofoam insulating layer, mounted onto the manual probe station. The enclosure was designed to be filled with liquid nitrogen through a dedicated inlet. A test chip containing *low-dose* Josephson junctions was glued to the bottom of the box using BF-6 Bakelite phenol-formaldehyde adhesive, and a Si-540 silicon diode thermometer was mounted nearby for temperature monitoring via a spare channel of the source-measurement unit. Electrical connections to the sample were made by inserting the manual station's probe needles through a large opening in the box lid, which also allowed nitrogen boil-off to escape and thereby suppressed condensation on the sample. A secondary gas inlet enabled controlled warmup using room-temperature nitrogen gas and provided a slight overpressure to mitigate moisture accumulation. Significant thermal contraction and expansion of the probe needles during cooldown and warmup required repeated manual realignment to maintain electrical contact with the sample.

Figure F1(a) shows an electrical tuning experiment of a 183-day-old *low-dose* junction, where the device is submerged in liquid nitrogen immediately after resistance

manipulation, so that relaxation occurs at lower temperatures. Remarkably, no resistance increase is observed while the junction remains cold.

To further emphasize that the relaxation-induced resistance increase halts at low temperature, we normalize the measured resistance to its room-temperature equivalent using an approximation to Simmon's model for tunneling through a thin insulator barrier,

$$G(T) = G_0 \cdot \left( 1 + \left( \frac{T}{T_0} \right)^2 \right) , \quad (\text{F.1})$$

where  $G_0$  and  $T_0$  are the characteristic conductance and characteristic temperature, respectively. This model is expected to be applicable since the junction never becomes superconducting during the experiment, and behaves as a metal-insulator-metal junction with a negative temperature coefficient. We find a conversion between the room-temperature conductance and the cryogenic conductance,

$$G_{\text{RT}}(T) = G_{\text{Cryo}}(T) \cdot \left( \frac{G_0 \cdot \left( 1 + \left( \frac{297[\text{K}]}{T_0} \right)^2 \right)}{G_0 \cdot \left( 1 + \left( \frac{T}{T_0} \right)^2 \right)} \right) , \quad (\text{F.2})$$

where  $1/G_{\text{Cryo}} = R$  is the resistance of the junction as we measure it in-situ. Both  $G_0$  and  $T_0$  are determined experimentally in figure F1(b), where three *low-dose* junctions are cooled down, while their resistance and temperature are continuously monitored without performing any electrical tuning. Fitting these three datasets to equation (F.1) yields an averaged normalized conductance  $\langle G_0 \rangle = 0.8791$ , and an averaged  $\langle T_0 \rangle = 779.5$  K.  $G_0$  would, in principle, correspond to the zero-temperature conductance of the junction; its inverse gives

$$1/\langle G_0 \rangle = R/R_N = 1.1375 , \quad (\text{F.3})$$

in close agreement with the  $R/R_N$  factor 1.1385 used throughout this work. Using  $\langle T_0 \rangle$  in equation (F.2), figure F1(a) shows the resulting temperature-corrected resistance, confirming that resistance relaxation is effectively frozen out at cryogenic temperature. Moreover, resistance relaxation resumes as the device thaws. It should also be mentioned that electrical tuning itself is known to speed up at elevated temperatures [22]

We initially suspected that the resistance increase observed during active manipulation arises from localized Joule heating at the junction's metal-insulator interface, caused by power dissipation  $P = V_{\text{drop}} \cdot I$ . In [42, figure 4.9], this hypothesis was tested by simulating the localized heating in a cross-style Josephson junction [43] under DC manipulation. For a representative case of  $V_a = 0.9$  V applied for 10 min, the junction dissipates approximately 110  $\mu\text{W}$  at the Al-AlO<sub>x</sub> interface. Assuming that 10% of the junction area participates in tunneling [28], the resulting tunnel current is 120  $\mu\text{A}$ , corresponding to a simulated local temperature rise of  $\sim 4$  K. This result is an order of magnitude below the levels required for conventional thermal annealing, and is also consistent with a recent study reporting  $\sim 8$  K local heating in comparable junctions [44].

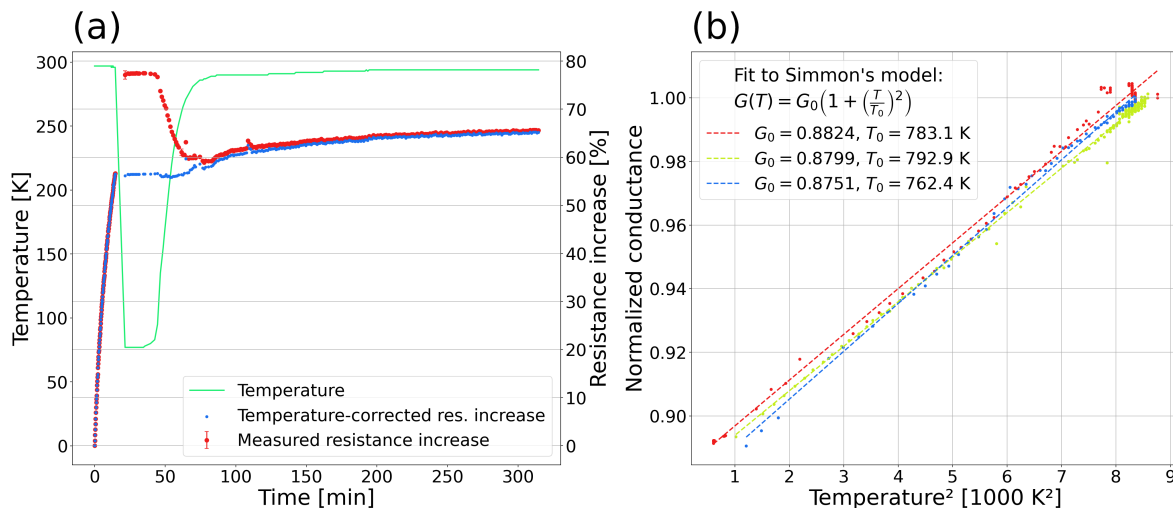


**Figure F1.** (a) Electrical tuning of a Josephson junction with the relaxation performed in liquid nitrogen. No resistance increase is observed while the junction remains cold, a result further emphasized by comparison with the temperature-corrected resistance trace shown as blue points. (b) Determination of the average characteristic temperature ( $T_0$ ) and normalized conductance ( $G_0$ ) used for the Simmon-model correction in equation (F.2), extracted from three liquid-nitrogen cooldowns in which temperature and conductance were monitored for three *low-dose* junctions

These results raise the question of whether the relaxation process is fundamentally distinct from, or closely related to, natural aging. Aging studies of Josephson junctions [14, 29] show that aging slows at lower temperatures, with their glassy relaxations showing the same trend [27]. Both aging and relaxation also share in common that subjecting the sample to sufficient heat halts further aging [14], as well as the ability to change resistance from electrical tuning [23]. The experimentally available evidence suggests a common physical origin being the redistribution of oxygen within the oxide barrier. In this picture, the electric field generated by the applied pulses locally modifies the potential landscape, enabling oxygen ions trapped in non-equilibrium sites to overcome energy barriers they could not surmount thermally at ambient temperatures. The observation that we successfully perform electrical tuning on samples older than one year further supports the interpretation that electrical tuning is not simply accelerated aging.

Recent hypotheses [22, 31] speculate that electrical tuning is related to field-assisted oxidation through the Cabrera-Mott mechanism [32]. Within this frame, electrical tuning accelerates the intrinsic relaxation dynamics of the junction not through heating, but by providing an electric-field-driven impulse that promotes ionic rearrangement toward a more stable configuration. However, this interpretation must be reconciled with experimental results showing that Cabrera-Mott oxidation increases as the temperature is lowered [45], in contrast to observations that electrical tuning speeds up with increased temperature.

## Appendix G. Dielectric breakdown

Figure G1 shows dielectric breakdown characteristics of *high-dose* junctions. In figure G1(a) the automated probe station was used to apply a current ramp to 119 junctions with areas ranging from  $150 \times 150 \text{ nm}^2$  to  $600 \times 600 \text{ nm}^2$ , while monitoring the voltage across them. The breakdown voltage  $V_{\text{break}}$  is defined as the highest voltage measured before the resistance dropped below  $260 \Omega$ , a threshold determined empirically as the upper bound for the short-circuit resistance of a failed junction. For junctions with electrode widths between 400 nm and 600 nm, we consistently observed  $V_{\text{break}} \approx 1.1 \text{ V}$ . As shown in figure G1(b), smaller junctions exhibit increased scatter in both breakdown voltage and resistance-area product, reflecting increased measurement uncertainty and device-to-device variability at reduced dimensions. These results indicate that, for each wafer, dielectric breakdown measurements on sacrificial junctions are essential for establishing safe upper bounds on the voltage amplitude used during electrical tuning.

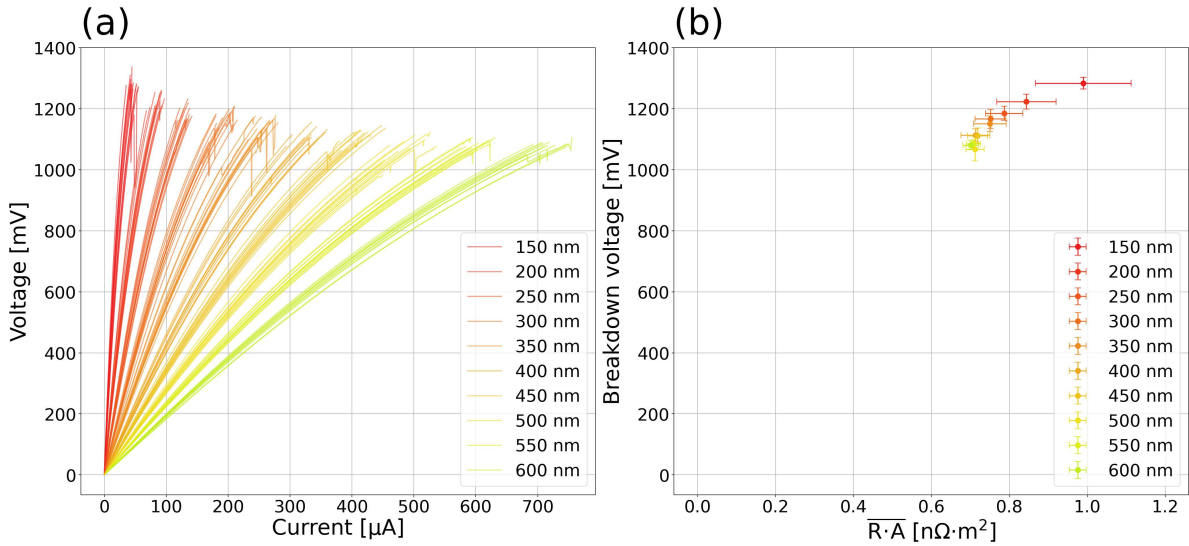


**Figure G1.** Current-ramped dielectric breakdown measurements performed on sacrificial Josephson junctions from the *high-dose* wafer. (a) Individual I-V curves for 119 junctions of different sizes. (b) Breakdown voltage as a function of the mean resistance-area product. The legends show the electrode width of the junctions.

## References

- [1] Blais A, Grimsmo A L, Girvin S M and Wallraff A 2021 *Reviews of Modern Physics* **93** URL <http://dx.doi.org/10.1103/RevModPhys.93.025005>
- [2] Josephson B D 1962 *Physics Letters* **1** 251–253 URL [http://dx.doi.org/10.1016/0031-9163\(62\)91369-0](http://dx.doi.org/10.1016/0031-9163(62)91369-0)
- [3] Anderson P W and Rowell J M 1963 *Physical Review Letters* **10** 230–232 URL <http://dx.doi.org/10.1103/PhysRevLett.10.230>
- [4] Muthusubramanian N, Finkel M, Duivesteyn P, Zachariadis C, van der Meer S L M, Veen H M, Beekman M W, Stavenga T, Bruno A and DiCarlo L 2024 *Quantum Science and Technology* **9** 025006 URL <http://dx.doi.org/10.1088/2058-9565/ad199c>
- [5] Moskalev D O, Zikiy E V, Pishchimova A A, Ezenkova D A, Smirnov N S, Ivanov A I, Korshakov N D and Rodionov I A 2023 *Scientific Reports* **13** URL <http://dx.doi.org/10.1038/s41598-023-31003-1>
- [6] Osman A, Fernández-Pendás J, Warren C, Kosen S, Scigliuzzo M, Frisk Kockum A, Tancredi G, Fadavi Roudsari A and Bylander J 2023 *Physical Review Research* **5** URL <http://dx.doi.org/10.1103/PhysRevResearch.5.043001>
- [7] Kreikebaum J M, O’Brien K P, Morvan A and Siddiqi I 2020 *Superconductor Science and Technology* **33** 06LT02 URL <http://dx.doi.org/10.1088/1361-6668/ab8617>
- [8] Pishchimova A A, Smirnov N S, Ezenkova D A, Krivko E A, Zikiy E V, Moskalev D O, Ivanov A I, Korshakov N D and Rodionov I A 2023 *Scientific Reports* **13** URL <http://dx.doi.org/10.1038/s41598-023-34051-9>
- [9] Osman A 2024 *Scaling Superconducting Quantum Processors: Coherence, Frequency Targeting and Crosstalk* Ph.D. dissertation, Chalmers University of Technology Gothenburg, Sweden ch. 2.5 URL <https://research.chalmers.se/en/publication/543784>
- [10] Hertzberg J B, Orcutt J S, Paik H, Rosenblatt S and Sandberg M O 2025 Frequency tuning of multi-qubit systems US Patent US12414482B2 URL <https://patents.google.com/patent/US12414482B2/en>
- [11] Hertzberg J B, Zhang E J, Rosenblatt S, Magesan E, Smolin J A, Yau J B, Adiga V P, Sandberg M, Brink M, Chow J M and Orcutt J S 2021 *npj Quantum Information* **7** URL <http://dx.doi.org/10.1038/s41534-021-00464-5>
- [12] Pavolotsky A B, Dochev D and Belitsky V 2011 *Journal of Applied Physics* **109** URL <http://dx.doi.org/10.1063/1.3532040>
- [13] Lehnert T, Billon D, Grassl C and Gundlach K H 1992 *Journal of Applied Physics* **72** 3165–3168 URL <http://dx.doi.org/10.1063/1.351479>
- [14] Koppinen P J, Väistö L M and Maasilta I J 2007 *Applied Physics Letters* **90** URL <http://dx.doi.org/10.1063/1.2437662>

- [15] Granata C, Vettoliere A, Petti L, Rippa M, Ruggiero B, Mormile P and Russo M 2007 *Applied Physics Letters* **90** URL <http://dx.doi.org/10.1063/1.2746060>
- [16] van der Meer S 2021 *Improving Frequency Targeting of Transmon Qubits Through Automated Laser Annealing* Master's thesis, Delft University of Technology accessed: 2025-07-11 URL <https://resolver.tudelft.nl/uuid:a1c52f6b-4882-4d4b-8423-4056973efa5e>
- [17] Zhang E J, Srinivasan S, Sundaresan N, Bogorin D F, Martin Y, Hertzberg J B, Timmerwilke J, Pritchett E J, Yau J B, Wang C, Landers W, Lewandowski E P, Narasgond A, Rosenblatt S, Keefe G A, Lauer I, Rothwell M B, McClure D T, Dial O E, Orcutt J S, Brink M and Chow J M 2022 *Science Advances* **8** URL <http://dx.doi.org/10.1126/sciadv.abi6690>
- [18] Groves T R 1996 *Journal of Vacuum Science & Technology B: Microelectronics and Nanometer Structures Processing, Measurement, and Phenomena* **14** 3839–3844 URL <http://dx.doi.org/10.1116/1.588678>
- [19] Balaji Y, Acharya N, Armstrong R, Crawford K G, Danilin S, Dixon T, Kennedy O W, Pothuraju R D, Shahbazi K and Shelly C D 2024 Electron-beam annealing of Josephson junctions for frequency tuning of quantum processors URL <https://arxiv.org/abs/2402.17395>
- [20] University of Chicago 2022 Technologies for tuning superconducting Josephson junctions, US Patent US20220140221A1 URL <https://patents.google.com/patent/US20220140221A1>
- [21] Nylander A and Rommel M 2024 System and Method for Trimming Metal-Insulator-Metal Junctions, International Patent Application WO2024225965A1, World Intellectual Property Organization URL <https://patents.google.com/patent/WO2024225965A1/en>
- [22] Pappas D P, Field M, Kopas C J, Howard J A, Wang X, Lachman E, Oh J, Zhou L, Gold A, Stiehl G M, Yadavalli K, Sete E A, Bestwick A, Kramer M J and Mutus J Y 2024 *Communications Materials* **5** URL <http://dx.doi.org/10.1038/s43246-024-00596-z>
- [23] Chaves K, Iaia V, Rash D, Rosen Y, Alegria L and Abelson A 2025 Oral: Expanded Parameter Search of Alternating-Bias Assisted Annealing (ABAA) presented by Loren Alegria at the APS Global Physics Summit, session MAR-C18: Advanced Fabrication for Superconducting Qubits, Anaheim Convention Center, Room 162 (level 1), March 17, 2025
- [24] Koch J, Yu T M, Gambetta J, Houck A A, Schuster D I, Majer J, Blais A, Devoret M H, Girvin S M and Schoelkopf R J 2007 *Physical Review A* **76** URL <http://dx.doi.org/10.1103/PhysRevA.76.042319>
- [25] Osman A 2019 *Reliability and Reproducibility of Josephson Junction Fabrication* Master's thesis, Chalmers University of Technology SE-412 96 Gothenburg, Sweden URL <https://hdl.handle.net/20.500.12380/302101>

- [26] Osman A, Simon J, Bengtsson A, Kosen S, Krantz P, P Lozano D, Scigliuzzo M, Delsing P, Bylander J and Fadavi Roudsari A 2021 *Applied Physics Letters* **118** URL <http://dx.doi.org/10.1063/5.0037093>
- [27] Nesbitt J R and Hebard A F 2007 *Physical Review B* **75** URL <http://dx.doi.org/10.1103/PhysRevB.75.195441>
- [28] Zeng L J, Nik S, Greibe T, Krantz P, Wilson C M, Delsing P and Olsson E 2015 *Journal of Physics D: Applied Physics* **48** 395308 URL <http://dx.doi.org/10.1088/0022-3727/48/39/395308>
- [29] Bladh K 2005 *Quantum Coherence in the Single Cooper Pair Box* Ph.D. dissertation, Chalmers University of Technology Gothenburg, Sweden
- [30] Pappas D, Field M, Sete E A, Mutus J Y and Wang X 2025 Voltage-assisted annealing to alter tunnel junction properties US Patent US20250204275A1 figures 5b, 8 and 9. URL <https://patents.google.com/patent/US20250204275A1>
- [31] Wang X, Howard J, Sete E A, Stiehl G, Kopas C, Poletto S, Wu X, Field M, Sharac N, Eckberg C, Cansizoglu H, Katta R, Mutus J, Bestwick A, Yadavalli K and Pappas D P 2024 Precision frequency tuning of tunable transmon qubits using alternating-bias assisted annealing *2024 IEEE International Conference on Quantum Computing and Engineering (QCE)* vol 01 (IEEE) pp 1315–1323 URL <http://dx.doi.org/10.1109/QCE60285.2024.00157>
- [32] Cabrera N and Mott N F 1949 *Reports on Progress in Physics* **12** 163–184 URL <http://dx.doi.org/10.1088/0034-4885/12/1/308>
- [33] Križan C and Toselli M 2025 *Dataset and code used for Electrical post-fabrication tuning of aluminum Josephson junctions at room-temperature* Zenodo open dataset URL <https://doi.org/10.5281/zenodo.17817324>
- [34] Tholén M O, Borgani R, Di Carlo G R, Bengtsson A, Križan C, Kudra M, Tancredi G, Bylander J, Delsing P, Gasparinetti S and Haviland D B 2022 *Review of Scientific Instruments* **93** URL <http://dx.doi.org/10.1063/5.0101398>
- [35] Tholén M O, Borgani R, Križan C, Bylander J and Haviland D B 2023 Characterization and benchmarking of a phase-sensitive two-qubit gate using direct digital synthesis arXiv:2308.08893 URL <https://arxiv.org/abs/2308.08893>
- [36] Ambegaokar V and Baratoff A 1963 *Physical Review Letters* **10** 486–489 URL <http://dx.doi.org/10.1103/PhysRevLett.10.486>
- [37] Ambegaokar V and Baratoff A 1963 *Physical Review Letters* **11** 104–104 Erratum URL <http://dx.doi.org/10.1103/PhysRevLett.11.104>
- [38] Rahamim J 2019 *Development of a Coaxial Circuit QED Architecture for Quantum Computing* Ph.D. dissertation, University of Oxford, Pembroke College trinity term URL <https://ora.ox.ac.uk/objects/uuid:c3311eef-7f31-4cfe-afd7-f3605b73ab36>
- [39] Didier N, Sete E A, da Silva M P and Rigetti C 2018 *Physical Review A* **97** URL <http://dx.doi.org/10.1103/PhysRevA.97.022330>

- [40] Mangin P and Kahn R 2017 *Cooper pairs - Principal results of BCS theory* (Cham, Switzerland: Springer International Publishing) p 214 ISBN 978-33-19505-27-5 URL [https://doi.org/10.1007/978-3-319-50527-5\\_9](https://doi.org/10.1007/978-3-319-50527-5_9)
- [41] Bardeen J, Cooper L N and Schrieffer J R 1957 *Physical Review* **108** 1175–1204 URL <http://dx.doi.org/10.1103/PhysRev.108.1175>
- [42] Toselli M 2024 *Post-fabrication Frequency Tuning in Superconducting Transmon Qubits* Master's thesis, Chalmers University of Technology, Gothenburg, Sweden URL <http://hdl.handle.net/20.500.12380/308503>
- [43] Potts A, Parker G, Baumberg J and de Groot P 2001 *IEE Proceedings - Science, Measurement and Technology* **148** 225–228 URL <https://digital-library.theiet.org/doi/10.1049/ip-smt%3A20010395>
- [44] Kennedy O W, Cole J H and Shelly C D 2025 Tuning of Josephson junctions – the effects of depinning physics arXiv:2502.18304 URL <https://doi.org/10.48550/arxiv.2502.18304>
- [45] Cai N, Zhou G, Müller K and Starr D E 2012 *Applied Physics Letters* **101** URL <http://dx.doi.org/10.1063/1.4764552>